

DIVERSE OXYGEN ISOTOPE VALUES AND HIGH MAGMATIC WATER
CONTENTS WITHIN THE VOLCANIC RECORD OF KLYUCHEVSKOY
VOLCANO, KAMCHATKA, RUSSIA

by

SARA LYNN AUER

A THESIS

Presented to the Department of Geological Sciences
and the Graduate School of the University of Oregon
in partial fulfillment of the requirements
for the degree of
Master of Science

December 2007

“Diverse Oxygen Isotope Values and High Magmatic Water Contents within the Volcanic Record of Klyuchevskoy Volcano, Kamchatka, Russia,” a thesis prepared by Sara Lynn Auer in partial fulfillment of the requirements for the Master of Science degree in the Department of Geological Sciences. This thesis has been approved and accepted by:

Dr. Paul Wallace, Chair of the Examining Committee

Date

11/26/07

Committee in Charge: Dr. Paul Wallace, Chair
 Dr. Ilya Bindeman
 Dr. Mark Reed

Accepted by:

Dean of the Graduate School

An Abstract of the Thesis of

Sara Lynn Auer for the degree of Master of Science

in the Department of Geological Sciences to be taken December 2007

Title: DIVERSE OXYGEN ISOTOPE VALUES AND HIGH MAGMATIC WATER
CONTENTS WITHIN THE VOLCANIC RECORD OF KLYUCHEVSKOY
VOLCANO, KAMCHATKA, RUSSIA

Approved: _____

Dr. Ilya Bindeman

Klyuchevskoy volcano, located in Kamchatka's subduction zone, is one of the most active arc volcanoes in the world and contains some of the highest $\delta^{18}\text{O}$ values for olivines and basalts. I present an oxygen isotope and melt inclusion study of olivine phenocrysts in conjunction with major and trace element analyses of ^{14}C and tephrochronologically-dated tephra layers and lavas spanning the eruptive history and the Al-Mg compositional range of the basalt to basaltic andesites found at Klyuchevskoy. A hybrid model of moderately-high $\delta^{18}\text{O}$ silicate melt from the subducting slab, coupled with high $\delta^{18}\text{O}$ fluid is provided to best explain Klyuchevskoy's 1) voluminous, high-rate volcanism, 2) unusual high- $\delta^{18}\text{O}$ signature, 3) two endmember basaltic magma, and, 4) hydrous high-Al, high- $\delta^{18}\text{O}$ component.

CURRICULUM VITAE

NAME OF AUTHOR: Sara Lynn Auer

PLACE OF BIRTH: Pigeon, Michigan

DATE OF BIRTH: June 22, 1983

GRADUATE AND UNDERGRADUATE SCHOOLS ATTENDED:

University of Oregon
Michigan State University

DEGREES AWARDED:

Master of Science, Geological Sciences, 2007, University of Oregon
Bachelor of Science, Geological Sciences, 2005, Michigan State
University

AREAS OF SPECIAL INTEREST:

Volcanology
Geochemistry

PROFESSIONAL EXPERIENCE:

Teaching Assistant, Department of Geological Sciences, University of
Oregon, Eugene, 2005-2007

Research Assistant, Department of Geological Sciences, University of
Oregon, Eugene, 2005-2007

GRANTS, AWARDS AND HONORS:

Graduate Research Grant, Oxygen isotope anomalies in Klyuchevskoy
Volcano, Kamchatka, Geological Society of America, 2006

ACKNOWLEDGMENTS

The investigation was supported in part by a grant from the National Science Foundation, # EAR0537872, to Dr. Ilya Bindeman at the University of Oregon and also by a Graduate Student Research grant from the Geological Society of America. I acknowledge Vera Ponomarova for her valuable assistance with sample collection and tephrochronology. Thank you to Maxim Portnyagin for providing ion microprobe analysis. Jim Palandri for providing valuable assistance in lasing samples.

To God, my foundation.

TABLE OF CONTENTS

Chapter	Page
I. INTRODUCTION	1
Part A: Geologic Overview of the Kamchatka Peninsula.....	1
1.1 Tectonic History of Kamchatka	1
1.2 Volcanic Zones of Kamchatka	3
1.3 Regional Geologic Structures	4
1.4 Volcanoes of the Central Kamchatka Depression “CKD”	5
1.5 Geochemistry and Mineralogy of the CKD.....	6
1.6 Tephrochronology	7
Part B: Geologic Overview of Klyuchevskoy Volcano.....	8
1.7 Geology and Magma Types	8
1.8 Oxygen Isotope Studies	10
1.9 Klyuchevskoy from a World Perspective	13
II. SAMPLING AND ANALYTICAL METHODS	14
2.1 Sampling of Klyuchevskoy Tephra and Lava	14
2.2 Analytical Methods	16
III. RESULTS	21
3.1 Lava and Tephra Record of Klyuchevskoy Volcano	21
3.2 $\delta^{18}\text{O}$ Evidence for Olivine Recycling	29
3.3 Fe-Mg Disequilibrium Between Olivines and Melt	33
3.4 Melt Inclusion Volatile Concentrations.....	35
3.5 Trace Element Variations in Melt Inclusions.....	43
IV. DISCUSSION	46
4.1 Olivine Recycling Processes Under Klyuchevskoy	46
4.2 Peridotite vs. Pyroxenite Source and Crustal Assimilation Models	47

Chapter	Page
4.3 Evidence for High H ₂ O Primary Melts Under Klyuchevskoy	52
4.4 Origin of High- $\delta^{18}\text{O}$ Peridotite Source Klyuchevskoy Magmas ..	53
4.5 Inheritance of High- $\delta^{18}\text{O}$ Signature from Prior Enrichment	57
4.6 Comparison with Mt. Shasta: A High- $\delta^{18}\text{O}$ H ₂ O-rich Volcano	59
V. CONCLUSIONS	62
APPENDICES	65
A. MAJOR AND TRACE ELEMENT ANALYSIS OF TEPHRA FROM KLYUCHEVSKOY VOLCANO	65
B. FIELD NOTES FROM SAMPLE COLLECTING AROUND KLYUCHEVSKOY VOLCANO JULY/AUGUST 2005	71
BIBLIOGRAPHY	75

LIST OF FIGURES

Figure	Page
1. Map of Kamchatka, Eastern Russia.....	1
2. Synthetic Cross-section of the Evolution of Kamchatka.....	2
3. Map of the Eastern Kamchatka Peninsula.....	4
4. Klyuchevskoy Aerial Photograph.....	8
5. Map of Klyuchevskoy.....	15
6. Field Photograph of Klyuchevskoy Tephra and Marker Ash Beds....	16
7. Generalized Stratigraphic Section.....	17
8. Compositional Variations of MgO and Al ₂ O ₃	21
9. Frequency of Klyuchevskoy Whole Rock Compositions.....	22
10. Compositional Variations Against Age.....	24
11. Isotopic Variations Against Age.....	25
12. $\delta^{18}\text{O}_{\text{olivine}}$ vs. MgO and Al ₂ O ₃	29
13. $\delta^{18}\text{O}_{\text{glass}}$ vs. MgO and Al ₂ O ₃	30
14. $\delta^{18}\text{O}_{\text{olivine}}$ vs. $\delta^{18}\text{O}_{\text{groundmass}}$	32
15. Olivine Groundmass Mg-Fe Equilibrium.....	33
16. Water Concentrations in MI vs. Compositional Parameters.....	35
17. H ₂ O vs. CO ₂ Concentrations in Melt Inclusions.....	42
18. Spider diagram of Trace Elements in Melt Inclusions.....	44
19. Trace Element Comparison of High-Al to High-Mg Samples.....	45
20. Trace Element Ratios in Olivines.....	48
21. $\delta^{18}\text{O}$ -SiO ₂ diagram.....	50
22. $\delta^{18}\text{O}$ -H ₂ O diagram.....	51
23. SiO ₂ -H ₂ O diagram.....	52
24. Mass Balance of Fluid or Melt Flux Melting.....	55
25. Schematic Diagram of the Evolution of Kamchatka.....	60

LIST OF TABLES

Table	Page
1. Oxygen Isotope Analyses	26
2. Composition of Melt Inclusions	36

CHAPTER I

INTRODUCTION

Part A: Geologic Overview of the Kamchatka Peninsula

1.1 Tectonic History of Kamchatka

The Kamchatka Peninsula, located in far eastern Russia, is an active component of the Pacific 'Ring of Fire' (**Figure 1**). The area has had a complex

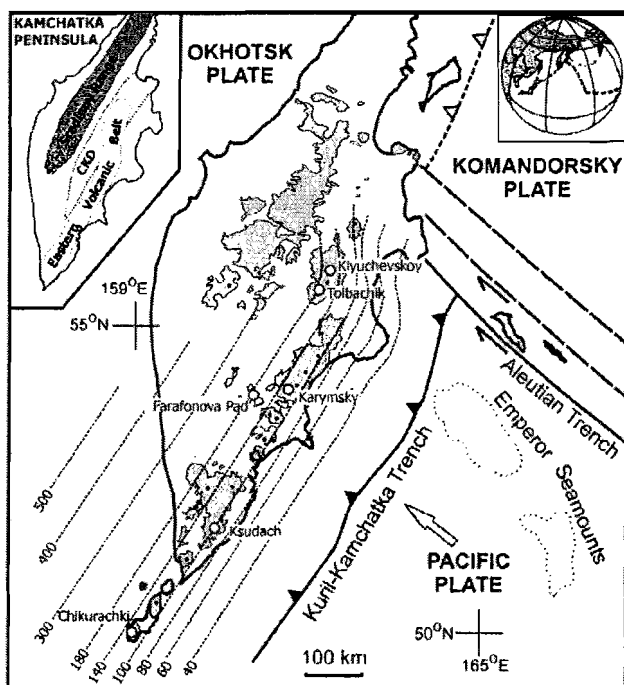


Figure 1. Map view of Kamchatka Peninsula, Eastern Russia. Three major volcanic zones are present: The Sredinny Ridge (SR), Central Kamchatka Depression (CKD), and the Eastern Volcanic Belt (EVB). Dashed lines indicate depth of the subducting Pacific plate below Kamchatka. Modified after Portnyagin et al. 2007b and Bindeman et al. 2004.

tectonic history as illustrated in **Figure 2**. Around 80 m.y.a. Kamchatka did not exist as we know it today. Instead the area was occupied from northwest to southeast by the Asian plate, the Eurasian plate, the Kula plate, and the Pacific plate. At this time there were two primary zones of subduction below the Kula plate: the Eurasian plate to the NW and the Pacific plate to the SE (**Figure 2a**; Konstantinovskaia 2000). Over

the next 20 m.y. this relationship continued until the transition of the Kula plate to encompass two spreading centers at the plate's NW and SE boundaries (**Figure 2b**). By the Early Eocene the Sredinny Massif, a proposed micro-continent from

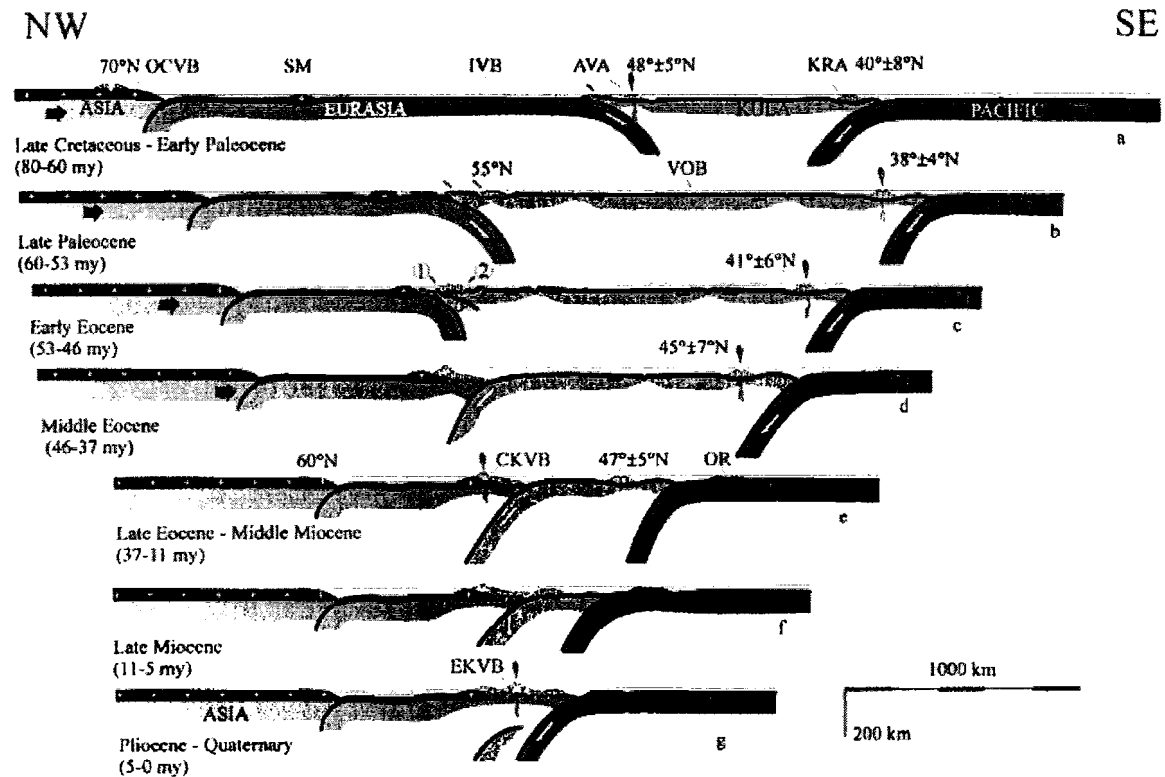


Figure 2. Synthetic cross-section of the evolution of Kamchatka through the interaction of the Asian continental margin, the Kula plate, and the Pacific Plate starting in the Late Cretaceous (~80 my) to the present. Primary features are: OCVB, Okhotsk–Chukotsky Volcanic Belt; SM, Sredinny Massif; IVB, Irunev–Valatuna oceanic Basin; AVA, Acahivayam–Valaginskaya arc; KRA, Kronotskaya arc; VOB, Vetlovka Oceanic Basin; ASIA, Asian Plate; EURASIA, Eurasian Plate; KULA, Kula plate; PACIFIC, Pacific plate; CKVB, Central Kamchatka Volcanic Belt; EKVB, Eastern Kamchatka Volcanic Belt. Adapted from Konstantinovskaia 2000.

the Sea of Okhotsk (Bindeman et al. 2002) located on the Eurasian plate, had accreted onto the northwestern section of the Kula plate essentially stalling subduction and forcing the subduction of the Kula plate below the Eurasian plate within the next 30 m.y. (**Figure 2 c-e** Konstantinovskaia 2000). By the Late Eocene the accreted terrain at the Eurasian-Kula plate boundary had become volcanically active and formed the Central Kamchatka Volcanic Belt. Accretion of

other terrains from the Kula plate continued eastwards until the Pliocene with the accretion of peninsulas onto Eastern Kamchatka, resulting in the locking of the subduction zone. This resulted in the break-off and sinking of the subducting Kula plate and subsequent subduction zone migration to the East, to its present location, with the Pacific plate subducting under the Asian plate. This transition initiated the formation of the Eastern Kamchatka Volcanic Belt (**Figure 2 f,g**; Konstantinovskaia 2000). As a result, today the Kamchatka peninsula is a complex jumble of accreted oceanic terrains, microcontinents, and accretionary wedges. These properties and their impact on volcanism are further examined in the following chapters.

1.2 Volcanic Zones of Kamchatka

Kamchatka's rich tectonic history is expressed in three main geologic regions (**Figure 3**): the accreted terrain of the Sredinny Massif, named the Sredinny Ridge to the northwest, the Eastern Volcanic Belt (EVB) to the southeast and the Central Kamchatka Depression (CKD), which falls between the two (Churikova et al. 2001; Dorendorf et al. 2000). The Sredinny Ridge was the most volcanically active until approximately 5 m.a. with the migration of the volcanic front to the east (**Figure 2 f-g**). Current volcanism in the region is represented by Khangar and Ichinsky volcanoes. As it has little bearing on this study, the Srdinny Ridge is not further discussed. The EVB, a ~100 km wide region parallel to the trench, is generally considered to be a frontal subduction-

related arc (Portnyagin et al. 2007b). The CKD, a 200 km wide graben feature, is home to some of the most active of Kamchatkan volcanoes, most notably the Klyuchevskoy Group volcanoes. The source of their voluminous volcanism is not yet well constrained but will be further examined in this study.

1.3 Regional Geologic Structures

At present Kamchatka is bordered by three plates: the Okhotsk plate to the west; the Komandorsky plate to the NE; and the Pacific plate to the SE. As shown in **Figure 3**, the boundary between the latter two plates is a series of fracture zones (FZ) with the Alpha FZ to the northeast, followed by the Bering FZ and Aleutian FZ to the southeast. The subducting Hawaii-Emperor Seamount

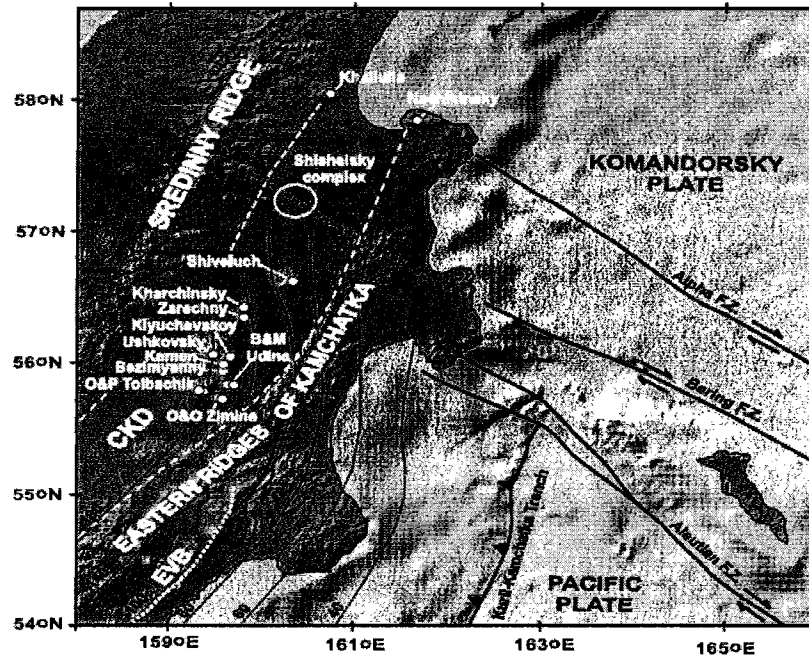


Figure 3. A map view of the eastern Kamchatka peninsula and local plate boundaries modified after Portnyagin et al. (2007b). White dashed lines indicate boundaries between volcanic zones. Short black dashed lines indicate inferred subducted plate depth below the crust. Solid black lines indicate major fracture zones. White circles represent volcanoes. EVB- Eastern Volcanic Belt; CKD-Central Kamchatka Depression.

Chain is located further to the SE of the Kurile-Kamchatka trench (Dorendorf et al. 2000) within the Pacific plate. The Pacific plate is subducting under the Eurasian plate at a fast rate of ~ 7.8 cm/yr at a moderate slab angle of 55° , which shallows to the north to around 25° (e.g. Gorbatov et al. 1997;1999). For the volcanic front this translates to a slab depth of ~ 100 - 140 km, while for the CKD volcanoes depths range from 140 - 180 km, although the slab shallows to a depth of ~ 100 km below Shiveluch, the northernmost active volcano, adjacent to the Aleutian trench (Portnyagin et al. 2007a).

1.4 Volcanoes of the Central Kamchatka Depression “CKD”

The CKD is host to well over a dozen volcanoes (**Figure 3**), with the largest cluster found at the Klyuchevskoy Group Volcanoes. Active volcanoes are all less than 50,000 years old (Dorendorf et al. 2000) and lay on a thick base of Middle to Late Pleistocene plateau basalts (Melekestsev 1980). The group includes active volcanoes such as Plosky Tolbachik and Bezymianny which abut Klyuchevskoy, the most active of the group, and the hydrothermally-active Ushkovsky volcano. Extinct volcanoes include Ostry Tolbachik, Malya and Bolshaya Udina, Ostaraya and Ovalanaya Zimina, and Kamen (Portnyagin et al. 2007b).

Adjacent to the Aleutian FZ, north of the Klyuchevskoy Group, is the Shiveluch Group volcanoes which consist of the highly active Shiveluch volcano and dormant Zarechny and Kharchinsky volcanoes. The next volcanic group, the

Shisheisky complex, is located inland of the Bering FZ approximately 50 km north the Shiveluch Group Volcanoes. At the northern extent of the CKD, and adjacent to the Alpha FZ, are Nachikinsky and Khailulia volcanoes. Volcanism related to the Shisheisky complex and Nachikinsky and Khailulia volcanoes is not directly subduction related and for the sake of relevance is not further discussed.

Seismic tomographic P-wave imaging of the Klyuchevskoy Group area shows a significant narrow P-wave anomaly from 20km depth which broadens at 30-40km below the edifice (Lees et al. 2007). Piyp and Yefimova (1993) infer this conical zone to be the primary magma source for the entire Klyuchevskoy group, with narrow conduits emanating from this source to smaller, secondary magma chambers for each individual volcano.

1.5 Geochemistry and Mineralogy of the CKD

Volcanoes of the CKD have not been uniformly researched and thus whole rock and mineral chemical analyses are skewed in favor of the most active and tectonically “interesting” volcanoes such as Klyuchevskoy, Tolbachik, Bezymianny, Shiveluch. Products from these Holocene volcanoes span a wide compositional range from medium-K and low- to medium-Fe basalts, which make up the majority of the rocks, to andesites of normal alkalinity (e.g. Kersting and Arculus 1994; Volynets 1994; Ariskin et al. 1995; Dorendorf et al. 2000; Ozerov 2000; Churikova et al. 2001; Mironov et al. 2001; Portnyagin et al. 2007b).

Locally, the base of the Klyuchevskoy group is composed of megaplagiophyric trachybasalts. This basalt is easily identified by the up to several

centimeter plagioclase crystals, which comprise up to 30% of the rock in hand sample. The edifice of Klyuchevskoy volcano, its predecessor Kamen volcano, and Bezymianny volcano are all medium-K basalts to basaltic andesites, respectively. Products range from high-Mg to high-Al within individual volcanoes. Klyuchevskoy and Kamen lavas and tephra contain olivine, pyroxene, and plagioclase phenocrysts whereas Bezymianny products contain pyroxene-plagioclase and amphibole-plagioclase assemblages (e.g. Kersting and Arculus 1994; Bindeman et al. 2004).

Volcanoes to the north, including Shiveluch, Zarechny, and Kharchinsky, (**Figure 3**) are composed of medium-to low-Fe, medium-K calc-alkaline basalts to andesites. The rocks are similar in major element composition to their neighbors in the south, although they are generally higher in MgO. Amphibole and Ca-rich pyroxene and olivine are common phenocryst phases in both andesitic and more primitive compositions (Portnyagin et al. 2007b).

1.6 Tephrochronology

Tephra from explosive Kamchatkan eruptions are found across the Kamchatka peninsula, providing tephra layers from numerous volcanoes in a single outcrop. Within the last two decades many of these ash layers have been ^{14}C dated (Braitseva et al. 1997). By identifying dated ash layers interspersed in tephra or lava deposits, age interval estimates of bracketed tephra or lava deposits can be determined. A single outcrop may contain thousands of years worth of volcanic deposits that can be sampled in a matter of days.

Eruptions providing these “marker beds” found in the Klyuchevskoy area include: 1955-56 and 2300 BP Bezymianny Volcano (BZ); periodic eruptions from 250-4800 BP at Shiveluch Volcano (SH); 1800 and 6000 BP Ksudach Volcano; 6600 Khungar Volcano (KHG); and 7550 Kizimen Volcano (KZ).

Part B: Geologic Overview of Klyuchevskoy Volcano

1.7 Klyuchevskoy Geology and Magma Types

Klyuchevskoy is the dominant volcano of the Klyuchevskoy Group Volcanoes, located in Kamchatka’s CKD (**Figure 4**). Its 4750 m high edifice consists of basaltic to basaltic andesitic tephra and lavas, and according to the ^{14}C dating of its basement formed entirely over the last ~7000 years

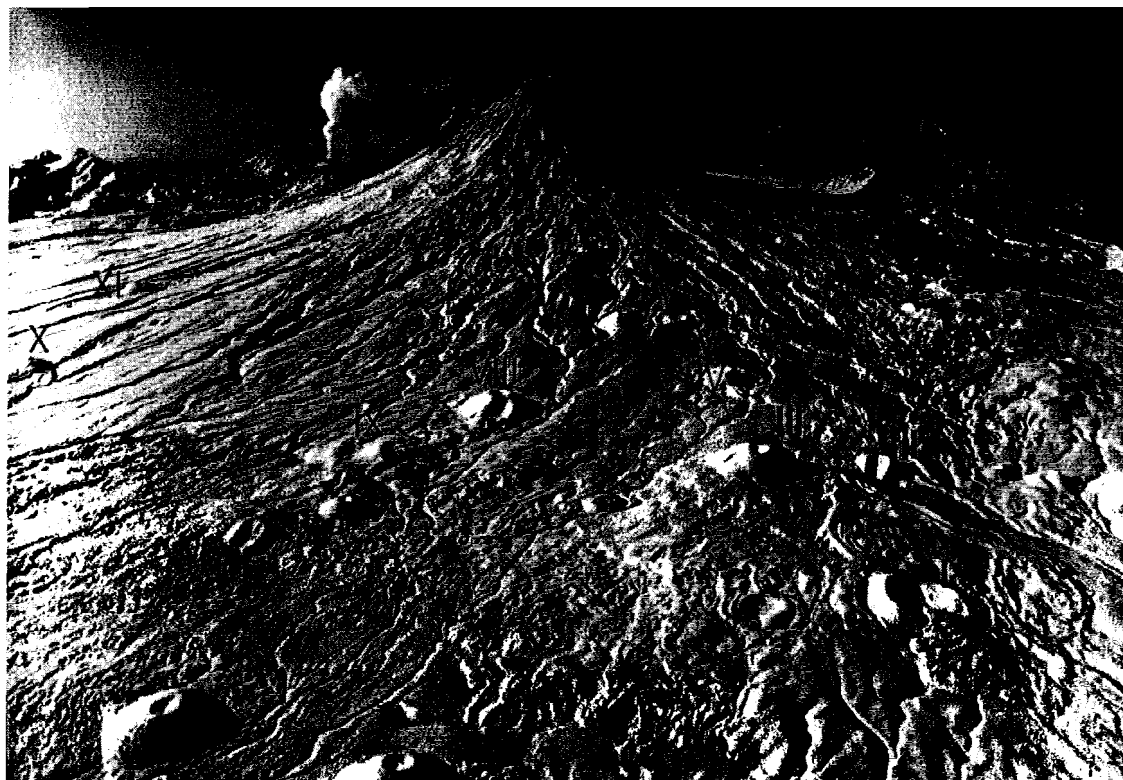


Figure 4. Klyuchevskoy Volcano aerial photograph of the north-east flank including satellite cones: I-Podkova, II-Lepyshka, III-Cone D, IV-Levashov, V-O, VI-E, VII-I, VIII-Ochki, IX-Biliukai, X-S. Photograph by Vasili Podtabachnyi.

(Melekestsev et al. 1980; Khrenov et al. 1991). Klyuchevskoy is built upon the flanks of the extinct basalt-andesite volcanoes of Kamen and Lavovy Shish, late Pleistocene shield volcanoes, and on the mid Pleistocene plateau basalts that serve as pedestal under most of giant stratacones in the Central Kamchatka Depression. Products more differentiated than basaltic andesites are not found at Klyuchevskoy, but are abundant at the neighboring Bezymianny volcano which shares common O, Sr, Pb, Nd isotopic characteristics with Klyuchevskoy (Bindeman et al. 2004; Almeev 2005) and may be supplied by the same mantle source as for Klyuchevskoy. The pre-Pleistocene basement under the CKD is made of mafic intra-oceanic accretionary terrain (Konstantinovskaia, 2001).

Klyuchevskoy is the most volcanically active of the group and possibly is the most active arc volcano on earth, yielding prolific magma production rates of 0.008 to 0.035 km³/yr (Khrenov et al. 1991). The voluminous volcanism in this area and the CKD in general cannot simply be explained by the fast rate of subduction (~7.8 cm/yr; e.g. Gorbatov et al. 1997;1999). Instead, substantial partial melting and/or fluid fluxing of the subducted thick hydrated crust (Kersting and Arculus 1994) of the Hawaii-Emperor Seamount chain has been called upon to explain this high rate of volcanism (Volynets 1994; Kersting and Arculus 1994; Dorendorf et al. 2000). Alternatively or in addition, an episode of “catastrophic slab loss” in the Pliocene (e.g. Levin et al. 2002), in which a portion of the subducted slab breaks off and sinks into the mantle (**Figure 2g**), is theorized to have caused hot mantle upwelling and mantle-lower crust interaction and melting, resulting in voluminous volcanism in the CKD. Mantle edge flow

(Yogodzinski et al. 2001) can explain slab melting and adakitic volcanism at northern CKD volcanoes such as Shiveluch, but Klyuchevskoy exhibits stronger subduction-flux-related trace element patterns (see Portnyagin et al. 2007a,b and below).

Klyuchevskoy basalts and basaltic andesites have been studied for several decades, resulting in the creation of several major and trace elemental databases (**Appendix A**; see also GEOROC website). Klyuchevskoy's volcanic rocks consist of both high-Mg and high-Al end members, as well as intermediate products. However, nearly all of the published analyses represent sampling of the same 10-20 historic to <200 BP lavas and scoria cones and repeated analyses of "prehistoric" Bulochka cone, the most magnesian, olivine-rich lava at Klyuchevskoy in the 2200-2700 BP range. Based on analyses of these lavas, Ariskin et al. (1995) has suggested that high-Mg basalts erupted earlier in the history of Klyuchevskoy and that later magmas were more differentiated (predominantly high-Al compositions).

1.8 Oxygen Isotope Studies

Motivation for this study stems from an effort to better understand the source of Klyuchevskoy's extremely high $\delta^{18}\text{O}$ values for basalts and their olivine phenocrysts, which have some of the highest $\delta^{18}\text{O}$ values in the world for arc volcanism. We used both lava and tephra to provide a chronologically extensive dataset so that we could investigate the $\delta^{18}\text{O}$ signatures of both phenocrysts and the melt (glass) over time.

Kersting (1991), Pineau et al. (1999), and Pokrovsky and Volynets (1999) reported $\delta^{18}\text{O}$ whole-rock values displaying a range of 5.5-8.5‰ (normal mantle derived melts values to up to 3‰ higher). Dorendorf et al. (2000), using the laser fluorination technique, found Klyuchevskoy lava-derived olivines range from 5.8 to 7.1‰ (0.4-1.7‰ higher than mantle-derived olivine) and suggested that these elevated $\delta^{18}\text{O}$ values reflect the involvement of high- $\delta^{18}\text{O}$ fluids derived from the subducted Hawaii-Emperor crust into the mantle wedge to produce melt. However, prohibitively large proportions of 20% or more (by weight) high $\delta^{18}\text{O}$ fluid are required in this model and thus time integration (i.e. multiple small additions) of $\delta^{18}\text{O}$ (but not water) would be needed. A second possibility is that this $\delta^{18}\text{O}$ enrichment could be linked to fractional crystallization and/or crustal assimilation of high $\delta^{18}\text{O}$ arc roots from accreted terrain such as amphibolite or other similar material (likely metamorphosed remnants of the Kula plate; Osipenko et al. 2007) beneath the CKD (Bindeman et al. 2004; Portnyagin et al. 2007a,b). A third possibility, the incorporation of subducted oceanic sediments, which have high $\delta^{18}\text{O}$ values due to low temperature reaction with seawater (Kersting and Arculus 1994, Muehlenbachs, 1986), could contribute to this $\delta^{18}\text{O}$ anomaly by providing high $\delta^{18}\text{O}$ sediment melt. However, Kersting and Arculus (1995) argued that a significant sediment contribution would result in the presence of radiogenic isotopes of Pb and Sr and non-radiogenic Nd in the magma source relative to MORB, which is not seen. Likewise, Volynets (1994) using ^{10}Be and the Tera date method (Tera et al. 1986), calculated subduction-

recycled sediment added to the mantle wedge beneath the Kamchatkan arc to be <1.5%. Duggen et al. (2007) offers an alternative explanation for the lack of a “sediment signature” in that current characterization of North Pacific sediments fails to take into account the possibility of a greater accumulation of volcanic ash in the sediment column closer to the subduction zone, which, if present, could create a different marine pelagic “sediment signature” than previously expected. Finally, Portnyagin et al. (2007b) suggested that a “dacite component” that results from slab melting is required to explain major and trace element features of mafic CKD magmas. They provide two basic models: (1) where dacitic slab melt and mantle melt mix to produce a pyroxenite which, at a later stage, undergoes further melting and mixing with mantle melts before reaching the plumbing system below CKD volcanoes; (2) slab dehydration triggers slab melting which in turn instigates mantle melting in a continuous reaction. Both models assume some shallow mixing/assimilation of lithospheric crust.

Here we present oxygen isotope analyses of olivine and matrix glass from throughout the eruptive history of Klyuchevskoy, with values ranging from 5.1-7.2‰ and 5.8-8.1‰, respectively. Major and trace element analyses of bulk tephra, olivine phenocrysts, olivine-hosted melt inclusions, and matrix glasses, are examined for crustal or subducted-slab-derived fluid signatures. The melt inclusion analyses also provide H₂O and CO₂ concentrations and approximate depths that reveal features of the plumbing system and crystallization processes beneath the volcano.

1.9 Klyuchevskoy from a World Perspective

Klyuchevskoy Volcano is not the only volcano in the world producing high- $\delta^{18}\text{O}$ olivine and magmas. Mount Shasta, located in the Northern California Cascade Arc (Grove et al. 2002; 2006), also shows elevated $\delta^{18}\text{O}_{\text{ol}}$ values ranging from 5.3‰ to 6.0‰ (i.e. as much as 1‰ higher than mantle-derived olivine values; Martin et al. in prep). Like Klyuchevskoy, Mt. Shasta is a very active volcano, located in a subduction zone setting, whose magmas are hydrous. Compositionally, Mt. Shasta rocks are more evolved (“high-Mg andesites”) than the surrounding area. Likewise, the majority of basalts in Klyuchevskoy are somewhat more silica rich than their counterparts elsewhere in the Central Kamchatka depression. High-Mg varieties of basalts contain 52-53 wt% SiO_2 and 10-12 wt% MgO, unlike the 47-48 wt% SiO_2 as is more commonly found for such a high MgO content. Therefore, it is useful to consider the components of subduction in the Cascade arc as they can be used to elucidate on the factors contributing to the substantial $\delta^{18}\text{O}$ enrichment at Klyuchevskoy.

CHAPTER II

SAMPLING AND ANALYTICAL METHODS

2.1 Sampling of Klyuchevskoy Tephra and Lava

Lavas available for sampling cover primarily the most recent 200 years of activity at Klyuchevskoy. These flows originated from the summit as well as flank vents at lower altitudes in the eastern half of the volcano (see **Appendix B** for lava flows sampled; **Figure 5**).

In this work we concentrate primarily on tephra, a product not studied by previous researchers. Tephra samples come from several riverbank outcrops around the NE quadrangle of Klyuchevskoy volcano and were deposited by both summit and parasitic cone eruptions (**Figure 5**). These ages range from historic deposits to those before the onset of Klyuchevskoy's cone (~7000 BP) up to 8500 BP. Major sample locations are denoted by stars in **Figure 5** and encompass the entire eruptive history of Klyuchevskoy.

Tephra layers range from a few millimeters to 1 m in thickness, which depends on the strength of the eruption, proximity of the vent, and the wind direction at the time of the eruption. Tephra layers are separated by clay-rich paleosols, and by lighter colored, more siliceous ash layers from distant Kamchatkan eruptions of known ^{14}C age (**Figure 6**). A relative chronology for these tephra layers has been established through their relation to "marker beds" (Braitseva et al. 1997) from major eruptions of volcanoes in the CKD, including:

Schiveluch and Bezymianny, as well as more distant volcanoes Ksudach, Kizimen, and Khangar. **Figure 7** gives a detailed stratigraphy of the sections we sampled and the marker beds that were used for tephrochronology.

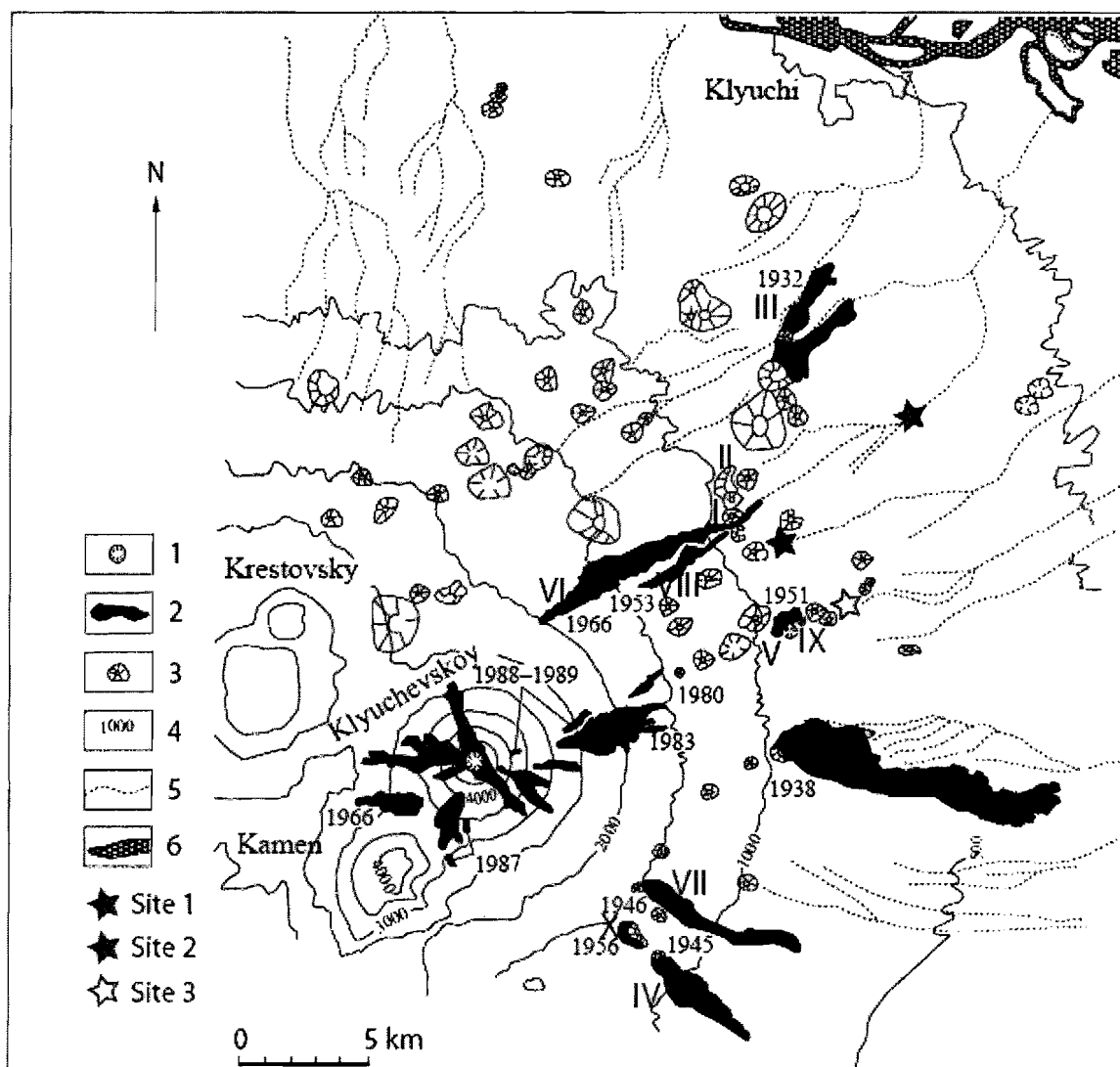


Figure 5. A map of Klyuchevskoy identifying: 1-Klyuchevskoy summit crater; 2-lava flows; 3-cinder cones; 4-contours; 5-dry river valleys; 6-Kamchatka River. Stars indicate our sampling sites, which include cinder cones and tephra layers spanning the exposed ~8500 yr eruptive history of Klyuchevskoy Volcano. Site 1- 300-75; Site 2-KLV 5; Site 3-KLV 15. Sampled lava flows include: I-Bulochka,II-Luchitsky, III-Tuyla,IV-Zavaritsky, V-Bylinkina, VI-Piip, VII-Apakhonchich, VIII-Belyankin, IX-Ochki, X-Vernadsky. See Appendix for exact locations. Map adapted from Ozerov et al. 1997.

Given the correlation of tephra layers, and their relative thickness and location with respect to the cones, an inference can be made in many cases



Figure 6. A field photograph of Klyuchevskoy tephra and marker ash beds. See Appendix B for code and age of marker tephra layer.

about the source of the tephra. Finer-grained, thinner tephra layers typically come from summit eruptions, while thicker coarser deposits are characteristic of local parasitic scoria cones. In this work we sampled only tephra layers thicker than 5cm, with lapilli of 1mm and larger which exhibit no sorting by water. Samples chosen for chemical analysis covered the chronological range of Klyuchevskoy. Sand sized and smaller particles were not analyzed due to the possibility of aeolian segregation and mixing of multiple deposits.

2.2 Analytical Methods

Oxygen isotope analyses were performed at the University of Oregon stable isotope lab using CO₂-laser fluorination. Individual and bulk mineral grains ranging in weight between 0.6 and 2 mg were reacted in the presence of purified BrF₅ reagent to liberate oxygen. The gas generated in the laser chamber was

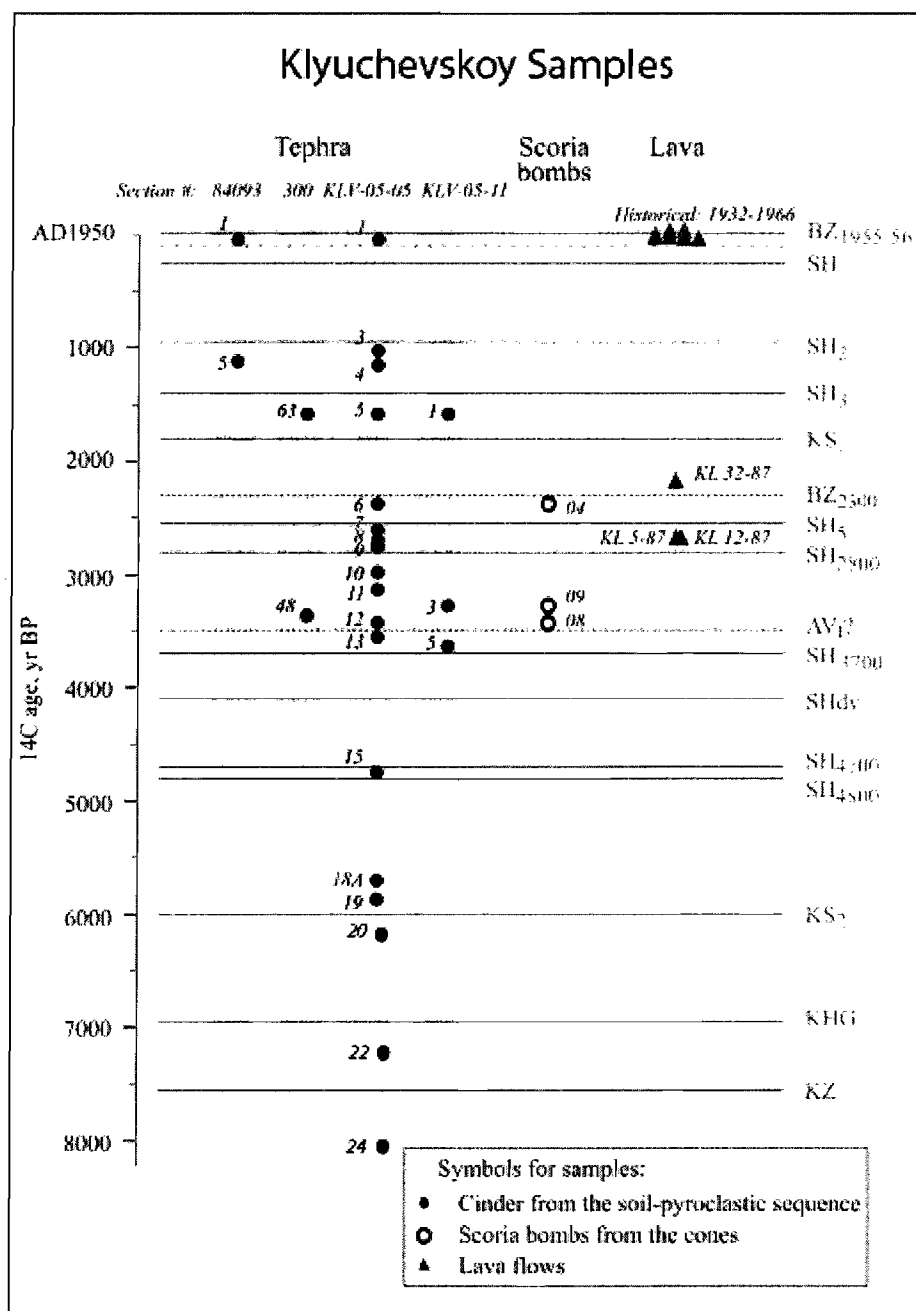


Figure 7. Generalized stratigraphic section and sampling of the tephra layers in four riverbank sections. Widespread, radiocarbon dated Holocene marker beds from explosive Kamchatkan eruptions are shown to the right. These beds were used to determine the age interval of studied eruptive products. Samples shown have major and trace element analyses given in Table 1. These samples fall in the range from the initiation of Klyuchevskoy activity of ~8500 BP-present. The earliest tephra of Klyuchevskoy sampled (# 24) overlies 1-10 m thick layer of glacial moraine, which overlies compositionally-different, megaplagiophytic lavas belonging to the subalkaline Lavovy Shish volcano, which predates modern Klyuchevskoy volcanism.

purified through a series of cryogenic traps held at liquid nitrogen temperature, and a mercury diffusion pump was used to remove traces of fluorine gas. Oxygen was converted to CO₂ gas in a small platinum-graphite converter, the yield was measured, and then CO₂ gas was analyzed on a MAT 253 mass spectrometer.

Four to seven standards were analyzed together with the unknowns during each analytical session. San Carlos olivine ($\delta^{18}\text{O} = 5.35\text{‰}$) and Gore Mt. Garnet ($\delta^{18}\text{O} = 5.75\text{‰}$) were used. Day-to-day $\delta^{18}\text{O}$ variability of standards ranged from 0.1 to 0.25‰ lighter than their empirical values. Measurements of unknowns were appropriately adjusted to correct for this variability. The precision on standards and duplicates of individual olivine analyses is better than 0.1‰.

Melt inclusions (MI) in olivine were analyzed for H₂O and CO₂ using Fourier Transform Infrared Spectroscopy (FTIR) at the University of Oregon. Over 40 melt inclusions in 7 tephra samples were identified, doubly intersected, and polished down to wafers 12-80 microns thick, depending on the size of the inclusion and olivine host. The thickness of each MI was determined by visual measurement under a petrographic microscope and in some cases by measurement of interference fringe spacing in reflectance spectra (Nichols and Wysoczanski 2007). The output of the FTIR analysis was the absorbance (A) of a particular species. Total dissolved H₂O was measured from the intensity of the asymmetric band at 3550 cm⁻¹ and dissolved CO₃⁻² was measured using peaks at 1515 and 1430. The concentration (c) of a species was then calculated using Beer's Law: $c = MA / \rho l \epsilon$, where M is the molecular weight of the species, ρ is the

density of the glass inclusion, l is the thickness of the inclusion, and ϵ is the molar absorption coefficient. The density was estimated initially by assuming an anhydrous composition, which was revised through calculation of the H₂O content of the glass and hydrous glass density (Ochs and Lange 1999). The molar absorption coefficient for H₂O used was 63 ± 3 L/mol cm (Dixon et al. 1995). Since the absorption coefficients for the carbonate doublet at 1515 and 1430 cm⁻¹ are compositionally dependant, they were calculated for each sample using the major element compositions of the melt inclusions and linear equations provided in Dixon and Pan (1995). Each melt inclusion was analyzed twice for accuracy. Corrections were made for post-entrapment crystallization of the melt inclusions (e.g. Sobolev and Shimizu 1993) with most inclusions receiving less than 4% olivine addition and with a maximum of 15%. Samples were also examined for iron loss (e.g. Danyushevsky et al. 2002), which was determined to be insubstantial for the melt inclusions studied.

Electron microprobe analyses of olivines and melt inclusions were performed at the University of Oregon on a Cameca SX100 electron microprobe, using 15kV accelerating voltage, 10 nA beam current, and a 10 um spot size for olivines and a 15 um spot size for melt inclusions to minimize sodium losses. Corrections for sodium loss were done by fitting observed count values vs. time with a best fit function, which can be used to extrapolate to time zero to determine actual Na₂O values. In order to obtain crystal free matrix glass for analysis, samples of matrix glass were heated briefly in the sample chamber under vacuum (~0 atm) using a high intensity laser to melt all of the phases.

These were then quenched by turning off power to the laser and analyzed on the electron microprobe.

Major and trace element whole rock X-ray fluorescence (XRF) analyses were performed at the GeoAnalytical lab at Washington State University on their ThermoARL Advant'XP+ sequential X-ray fluorescence spectrometer, except for the analyses of lavas that were earlier analyzed by XRF at GEOMAR.

Secondary Ion Mass Spectroscopy (SIMS) analyses of selected melt inclusions were done at the Leibniz Institute of Marine Sciences (IFM-GEOMAR) in Yaroslavl', Russia using a Cameca 4f ion microprobe using O²⁺ oxygen primary beam and energy filtering to resolve isobar interferences on oxides of heavy REE on light REE.

CHAPTER III

RESULTS

3.1 Lava and Tephra Record of Klyuchevskoy Volcano

Whole rock MgO and Al₂O₃ data for Klyuchevskoy tephra show two distinct endmembers of basalt: High-Mg (8-11 wt% MgO), and high-Al (17-19 wt% Al₂O₃, 3-6.5 wt% MgO), with intermediate basalt (6.5-8 wt% MgO, 15-17 wt% Al₂O₃) in between (Figure 8, Appendix A). These data overlap with previously published

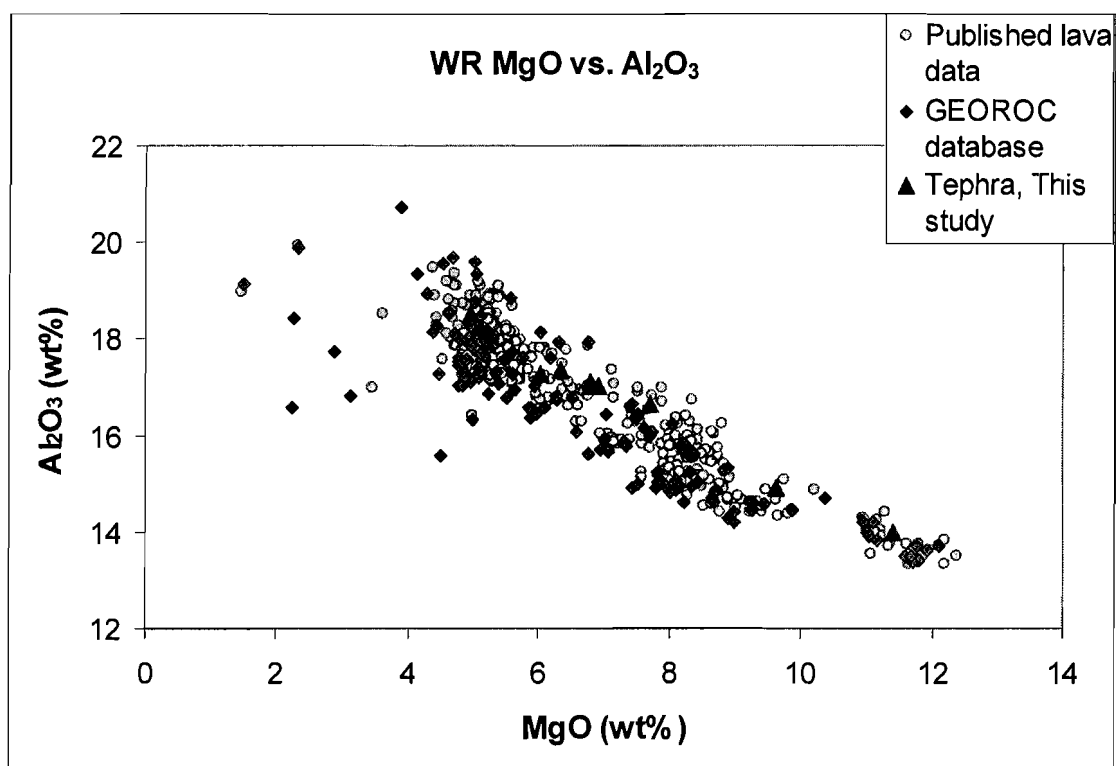


Figure 8. Compositional variations of MgO and Al₂O₃ within collected lava samples and tephra (this study) throughout the eruptive history of Klyuchevskoy. There is a clear negative correlation between MgO and Al₂O₃ and an overlap between analysis of samples presented here and published data (Portnyagin et al. 2007, GEOROC data is from <http://georoc.mpch-mainz.gwdg.de/georoc/Entry.html>).

analyses of lavas (**Figure 8**). To confirm the presence of these compositional groups we have plotted histograms (**Figure 9**) of all published analyses of Klyuchevskoy rocks from the GEOROC database in addition to recently published data from Portnyagin et al. (2007a,b) and data from this study.

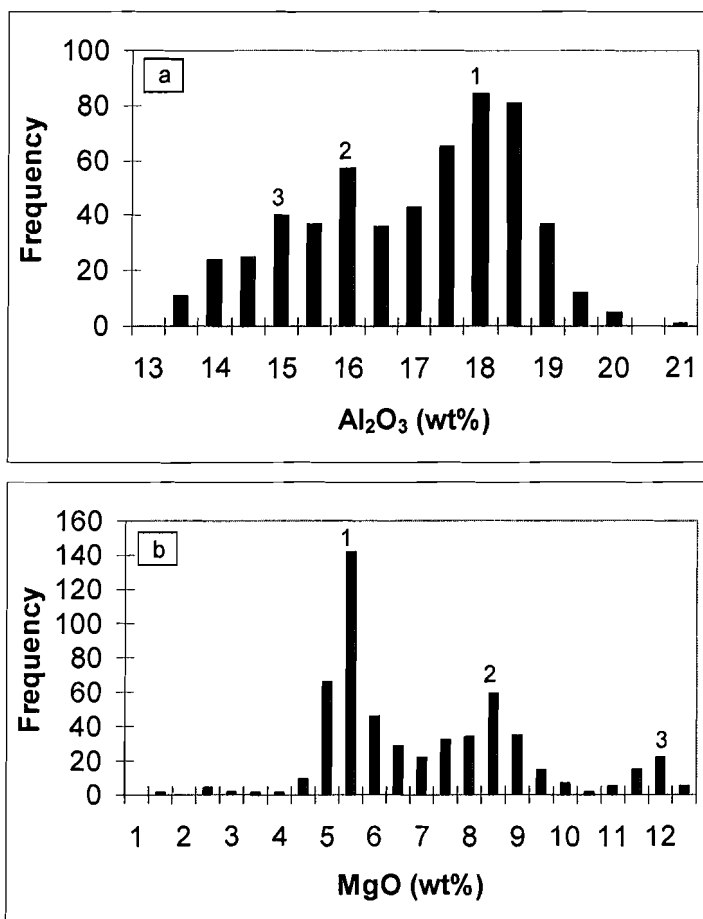


Figure 9. Frequency of Klyuchevskoy whole rock compositions for (a) Al₂O₃ and (b) MgO (wt%). Data is from this study and compiled from the GEOROC database and Portnyagin et al. (2007).

We find three maxima on the MgO and Al₂O₃ histograms, two corresponding to the above-defined high-Mg and high-Al compositional groups based on tephra, while the third maximum relates to the separate group of samples with the highest MgO and ~Fo₈₈ olivine. This group has likely formed due to olivine accumulation.

Our data demonstrates that high-Mg and high-Al end

members erupted throughout the history of Klyuchevskoy (**Figure 10**). In the lava record it has been observed that high-Al and high-Mg lavas occurred together in the same eruption (e.g. 1951 Bylinkinoi lava; Khubunaya 2007). The majority of our tephra samples are, however, high-Al. In our extensive

tephrachronological record, we find no distinct geochemical trend relating age of the volcanic material to MgO, Al₂O₃, or $\delta^{18}\text{O}$ (**Appendix A, Figure 10, 11**).

Nearly all of the samples from these compositional groups are enriched in $\delta^{18}\text{O}$ with respect to mantle values, with high-Al to intermediate basalt being the most enriched at 7.7-8.1‰, which is >2‰ higher than mantle melts (**Table 1, Figure 11**).

Bulk and individual olivine analyses fail to exhibit trends with composition, although $\delta^{18}\text{O}$ values are enriched from 5.1‰ to 7.3‰, up to 2.1‰ higher than normal mantle olivine (**Figure 12**). Basaltic glass shows a trend of increasing $\delta^{18}\text{O}$ with increasing Al₂O₃ and decreasing with MgO (**Figures 13 a, b**), but there is considerable scattering and relatively low R² values for plotted trendlines for olivine from tephra. However, the trend is better shown in olivine from lavas.

Fractional crystallization has been proposed by Ariskin et al. (1995) to account for this range in magma compositions. However, the potential for $\delta^{18}\text{O}$ enrichment of residual melts formed by fractional crystallization is ~0.3‰ (e.g., Bindeman et al. 2004) and is nowhere near the ~1 to 1.5‰ $\delta^{18}\text{O}$ increase seen at Klyuchevskoy, ruling out the possibility of fractional crystallization of high-Mg basalt as a viable solution. Another hypothesis for the high $\delta^{18}\text{O}$ magmas would be combined assimilation and fractional crystallization involving the incorporation of high- $\delta^{18}\text{O}$ amphibolite, which is further examined using mass balance calculations in section 4.2.

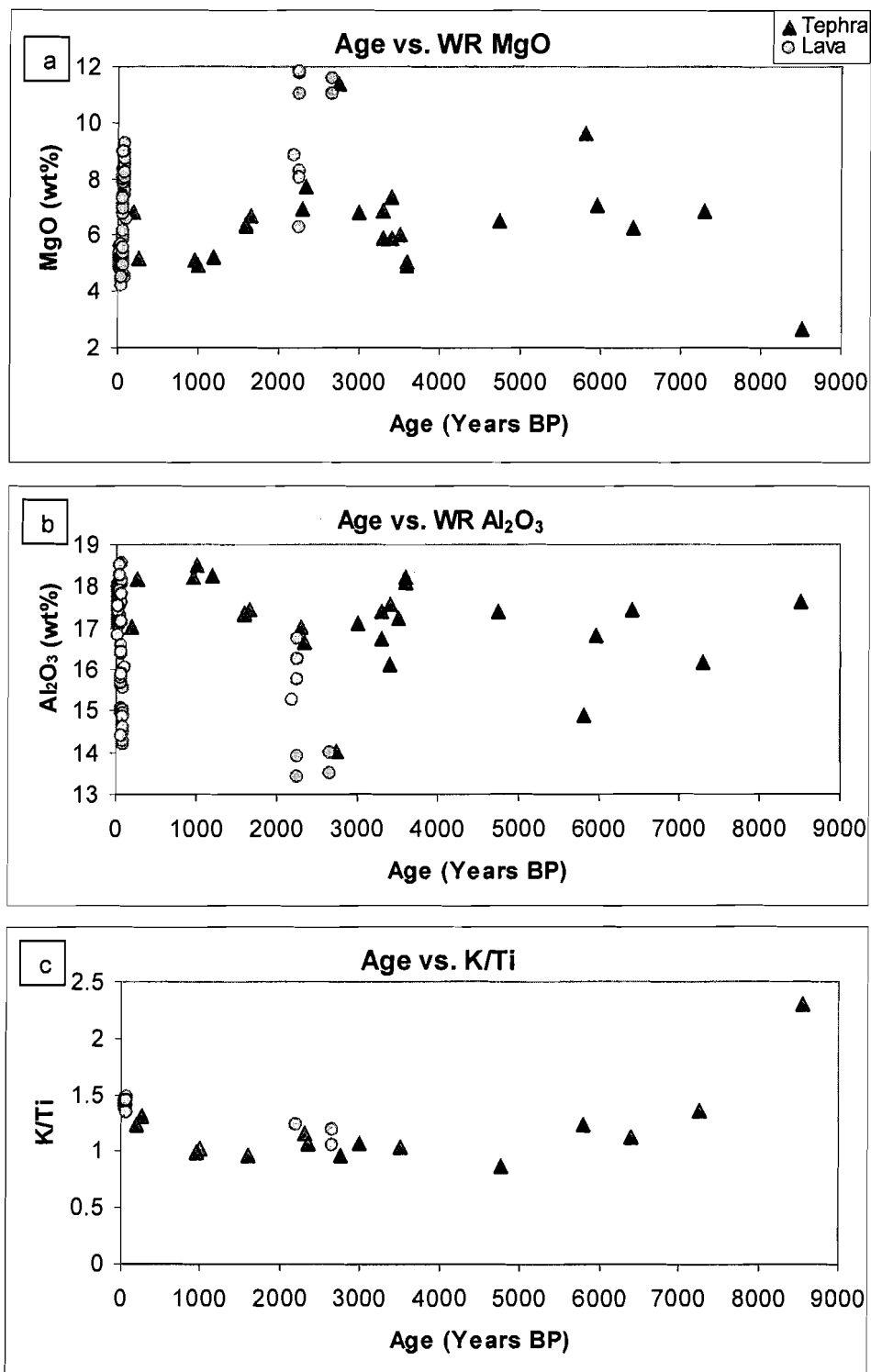


Figure 10. Compositional variations against age. A) MgO; B) Al₂O₃; C) K/Ti; These diagrams plot tephra samples vs. previously published lava samples (Portnyagin et al. 2007a,b; GEOROC database). No evolutionary trends are evident and analyses of tephra and lava overlap.

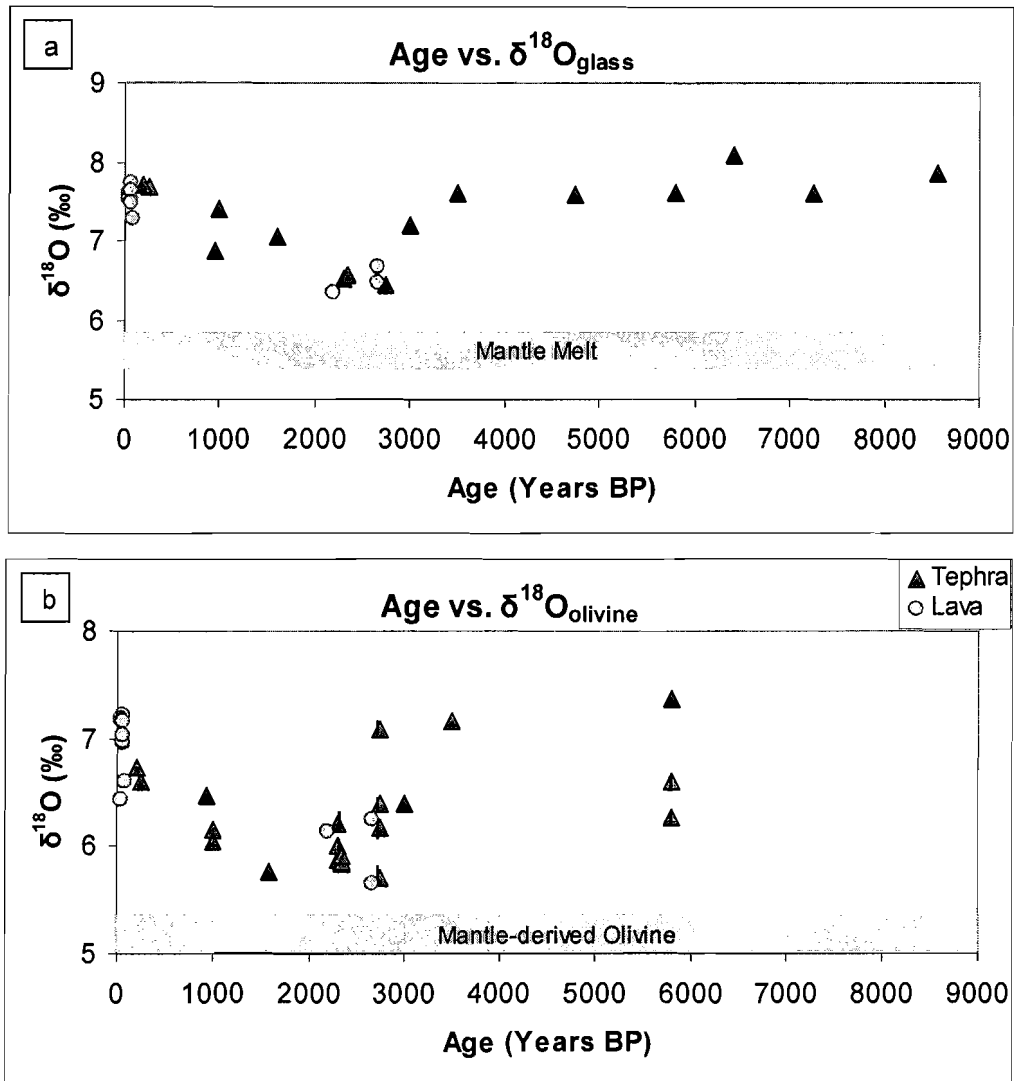


Figure 11. Isotopic variations against age. A) $\delta^{18}\text{O}$ glass and B) $\delta^{18}\text{O}$ olivine. This diagram plots tephra samples from this study vs. previously published lava samples (Portnyagin et al. 2007a,b). Olivine from both tephra and lava are enriched in $\delta^{18}\text{O}$ by up to 2‰. No evolutionary trends of isotopic values with age are evident. These plots, along with Figure 10, suggest coeval eruption and mixing of high-Al, high-Mg, and high- $\delta^{18}\text{O}$ and low- $\delta^{18}\text{O}$ basalts, tephra or lavas in geologic record of Klyuchevskoy volcano.

Table 1. Oxygen isotope analyses on individual and bulk phenocrysts and groundmass glass from Klyuchevskoy Volcano.						
OI is bulk olivine analysis; OI-# indicates number of olivine per analysis						
See Appendices A & B and Figure 3 for sample locality and chemical composition						
<i>Italicized values of extreme outliers were not used in Std Error calculations</i>						
Sample	Type	$\delta^{18}\text{O}$ olivine	$\delta^{18}\text{O}$ glass	Std Err (N) glass	~Age years BP	Flow/Tephra Section
840-93/1-5	ol	6.73	7.71	0.12 (2)	200	Site 1
KLV 4	ol-1	6.21			2300	Cone D
KLV 4	ol	5.88			2300	Cone D
KLV 4	ol-1	6.00			2300	Cone D
KLV 4	ol-1	5.13	6.51	0.15 (6)	2300	Cone D
KLV 5/1	ol	6.60	7.68	0.02 (2)	50	Site 2
KLV 5/3	ol	6.15			1100	Site 2
KLV 5/3	ol	6.04	7.40	0.11 (2)	1100	
KLV 5/4	ol	7.62	7.38	0.11 (5)	1200	Site 2
KLV 5/6	ol-1	5.84			2500	Site 2
KLV 5/6	ol-1	5.86			2500	Site 2
KLV 5/6	ol-1	5.92	6.58	0.07 (2)	2500	Site 2
KLV 5/7	ol	5.76			2600	Site 2
KLV 5/8	ol-1	6.18			2650	Site 2
KLV 5/8	ol-1	6.40			2650	Site 2
KLV 5/8	ol-1	7.08			2650	Site 2
KLV 5/8	ol-1	5.70	6.44	0.11 (6)	2650	Site 2
KLV 5/9	ol	6.09			2700	Site 2
KLV 5/9	ol-1	5.52			2700	Site 2
KLV 5/10	ol-1	6.40			3000	Site 2
KLV 5/10	ol-7	5.26	7.21	0.05 (2)	3000	Site 2
KLV 5/11	ol-2	6.26			3100	Site 2

Sample	Type	$\delta^{18}\text{O}$ olivine	$\delta^{18}\text{O}$ glass	Std Err glass	~Age Years BP	Flow/Cone
KLV 5/11	ol-2	6.19	7.06	0.04 (2)	3100	Site 2
KLV 5/15			7.58	0.09 (2)	4750	Site 2
KLV 5/18a	ol-1	6.27	7.53	0.12 (5)	5700	Site 2
KLV 5/18a	ol-1	6.61			5700	Site 2
KLV 5/18a	ol-1	7.37			5700	Site 2
KLV 5/20		nd	8.08	0.01 (2)	6400	Site 2
KLV 5/22		nd	7.61	0.14 (2)	7250	Site 2
KLV 5/24		nd	7.86	0.07 (2)	8550	Site 2
840-93/5-18	ol	6.47	6.60	0.08 (4) 5.83, 6.00	1100	Site 1
300-48	ol	7.16	7.60	0.13 (2)	3500	Site 1
300-5/63	ol	5.77	6.93	0.13 (3)	1600	Site 1
AP 60-31	ol	7.21	7.47	0.07 (3)	62	Apakhonchich
AP 60-31	ol-1	7.04			62	Apakhonchich
AP 60-31	ol	6.96			62	Apakhonchich
AP 60-31	ol	6.98			62	Apakhonchich
Bel 70-46	ol	7.17	7.62	0.01 (2)	54	Belyankinoi
Bel 70-46	ol	7.13			54	Belyankinoi
Byl 69-38	ol	6.98	7.74	0.01 (2)	56	Bylinkinoi
Byl 69-38	ol	6.98			56	Bylinkinoi
KL 5-87	ol	6.25	6.40	0.12 (3)	2650	Bulochka
KL 5-87	ol	6.03			2650	Bulochka
KLV 10			6.58	0.14 (2)	2650	Bulochka
KL 12-87	ol	5.65	6.66	0.06 (2)	2650	Luchitsky

Sample	Type	$\delta^{18}\text{O}$ olivine	$\delta^{18}\text{O}$ glass	Std Err glass	~Age Years BP	Flow/Cone
KL 32-87	ol	6.13	6.36	0.03 (3)	2200	Ochki
KL 32-87	ol	6.36			2200	Ochki
KL 45-87	ol	6.13	7.28	0.01 (2)	75	Tuyla
KL 45-87	ol	6.94			75	Tuyla
Piip 79-50	ol	6.44	7.60	0.02 (2)	41	Piip
KLV 6			7.09	0.16 (3)	41	Piip
V68-37	ol	7.18	7.51	0.05 (3)	51	Vernadsky
V68-37	ol	7.07			51	Vernadsky
Zav 50-49	ol-1	7.04	7.49	0.00 (2)	62	Zavaritsky

3.2 $\delta^{18}\text{O}$ Evidence for Olivine Recycling

The wide range of individual olivine $\delta^{18}\text{O}$ values within a single sample in this study demonstrates potential disequilibrium relations between their host glasses (**Figure 12**). However, the extent of disequilibria and heterogeneity of olivine $\delta^{18}\text{O}$ varies from sample to sample: whereas many olivine samples have a narrow $\delta^{18}\text{O}$ range, some samples have olivine $\delta^{18}\text{O}$ values that range up to 1‰.

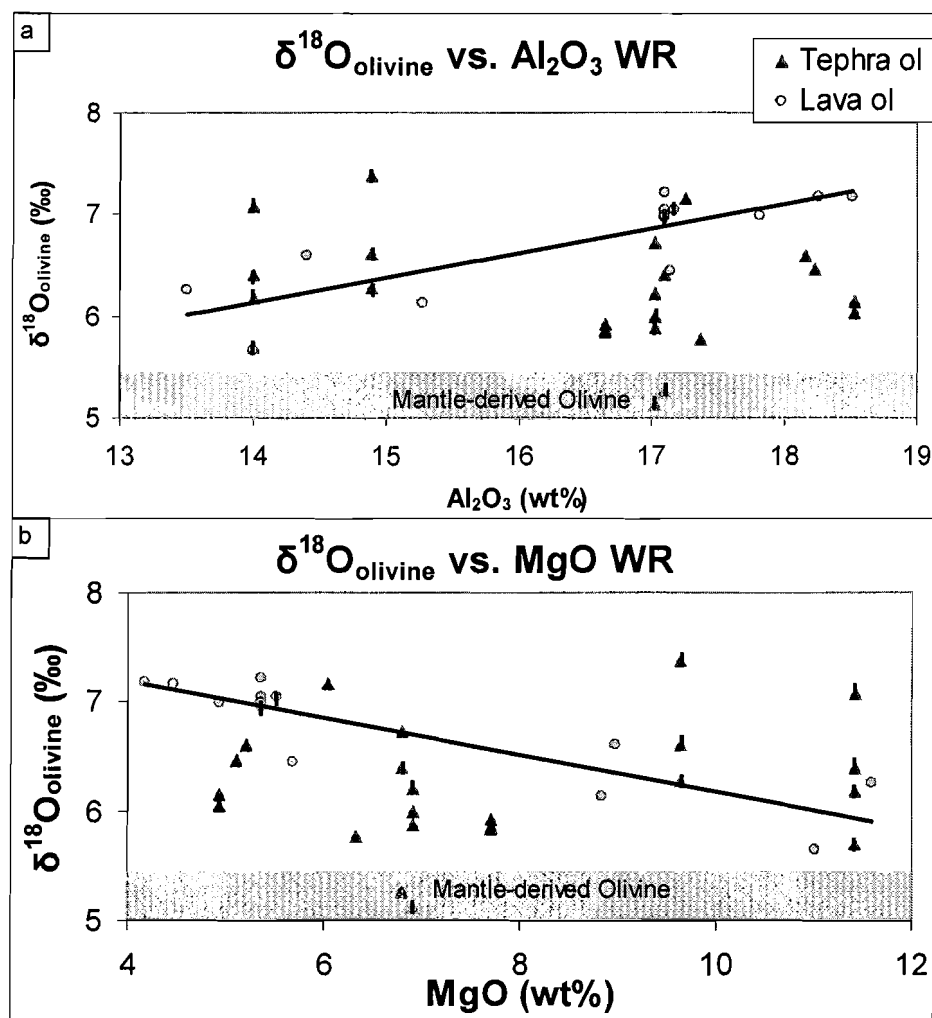


Figure 12. $\delta^{18}\text{O}_{\text{olivine}}$ vs. MgO and Al_2O_3 . Individual olivine phenocrysts (vertical line in samples) exhibit a high $\delta^{18}\text{O}$ range; bulk olivine analysis (symbols with no vertical line) reflect averaging of these diverse $\delta^{18}\text{O}$ individual analyses. Trend lines represent olivine from lavas and show a) an increase of $\delta^{18}\text{O}$ with Al_2O_3 and b) a decrease of $\delta^{18}\text{O}$ with MgO (R^2 values of 0.6831 and 0.7642 respectively). Tephra olivine show a similar, though weaker trend. This olivine $\delta^{18}\text{O}$ range is likely due to olivine recycling through magma mixing and cumulate addition.

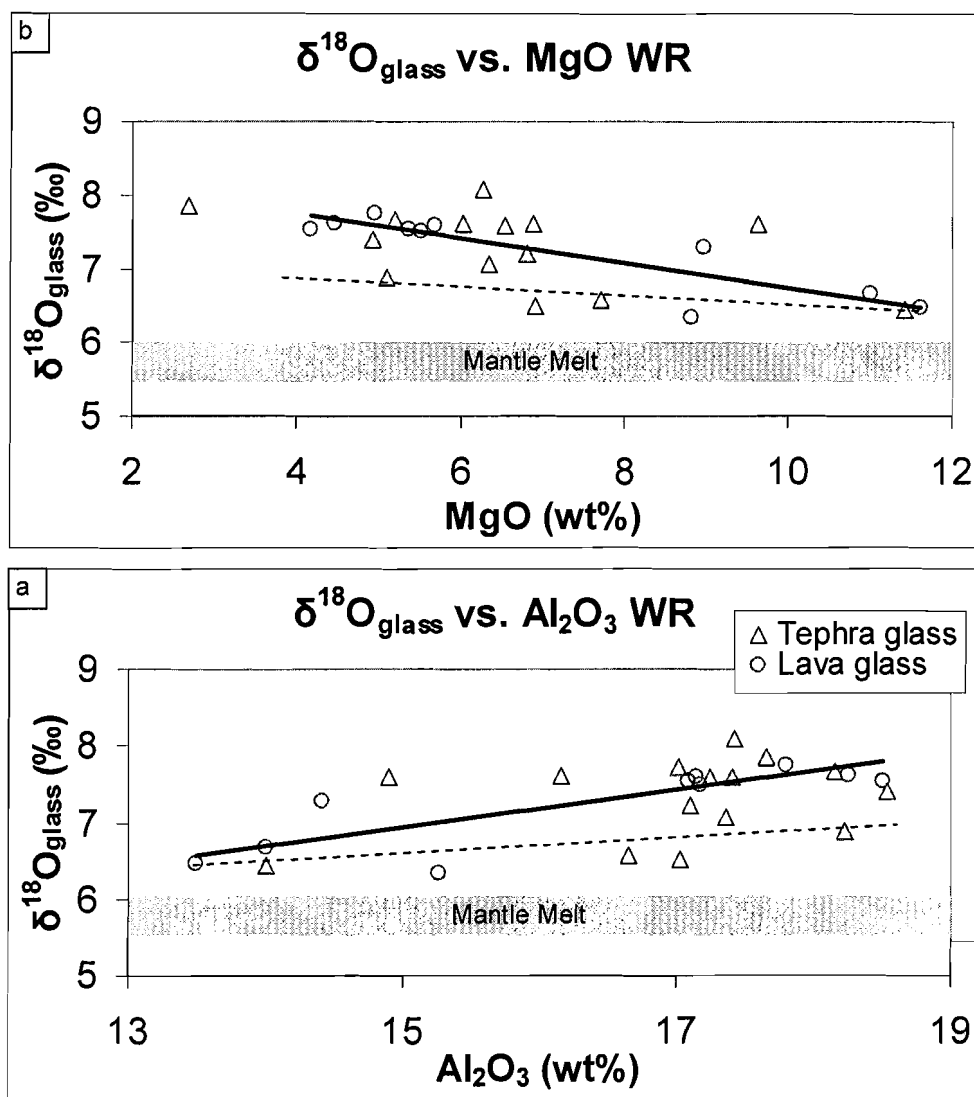


Figure 13. $\delta^{18}\text{O}_{\text{glass}}$ vs. MgO and Al_2O_3 . Both high-Al and high-Mg basalts are significantly higher in $\delta^{18}\text{O}$ than the mantle, with high-Mg basalts being $\sim 1\%$ higher, and high-Al being $\sim 2\%$ higher. Notice, a negative correlation is present for (a) $\delta^{18}\text{O}_{\text{glass}}$ and MgO and (b) a positive correlation of Al_2O_3 with $\delta^{18}\text{O}_{\text{glass}}$, with R^2 values for lava of 0.6934 and 0.7876 respectively. Slightly less of a correlation is present for tephra samples. The dashed line represents possible $\delta^{18}\text{O}$ enrichment due to fractional crystallization of a single parental moderately high- $\delta^{18}\text{O}$, high-Mg basalt. Fractionation can only account for up to a 0.3% increase, clearly not enough to account for the high- $\delta^{18}\text{O}$ basalts of Klyuchevskoy.

In order to examine isotopic equilibrium/disequilibrium between olivines and their host groundmass glass (**Figure 14**) we had to estimate olivine-melt oxygen fractionation factors. The first step in determining these factors was to separate the melt into mineral components (C.I.P.W. normative mineralogy) for which there are known forsterite-mineral fractionation factors. The C.I.P.W norm calculations were done using the whole-rock major element chemistry for each sample and following the method determined by Kelsey (1965).

Using the C.I.P.W. normative mineral proportions (A) for each sample were determined. Corresponding experimental mineral-forsterite isotope fractionation coefficients (Chiba et al. 1989) were determined for each normative component. These coefficients were then used to calculate the isotope equilibrium between the melt (sum of all mineral components) and olivine in the following equation: $1000 \ln \alpha = \Delta^{18}\text{O}_{\text{melt-olivine}} = \sum (A \cdot W \cdot 10^6 T^{-2})$; where T is estimated temperature of crystallization, W is the weight fraction of each normative mineral, and the sum of all the W's are equal to 1. For example, if a sample is found to have 20% mineral X, 30% mineral Y, and 50% mineral Z, the resulting equation would be: $\Delta^{18}\text{O}_{\text{melt-olivine}} = A_{\text{mineral X-Fo}} \cdot 0.2 \cdot 10^6 T^{-2} + A_{\text{mineral Y-Fo}} \cdot 0.3 \cdot 10^6 T^{-2} + A_{\text{mineral Z-Fo}} \cdot 0.5 \cdot 10^6 T^{-2}$.

Crystallization temperatures of 1100-1250°C estimated with the MELTS program (Ghiorso and Sack 1995) were used. Despite this range of temperature, a limited $\Delta^{18}\text{O}$ (melt-olivine) range was found. The melt-olivine isotope fractionation for high-Mg samples with a crystallization temperature around 1140°C was around 0.7‰, whereas high-Al and intermediate composition

samples was around 0.8‰. Olivines ranged from being in isotopic equilibrium to being up to 1.2‰ lighter to 1.5‰ heavier than the groundmass. This range of isotopic disequilibrium is determined to be due to recycling (mixing) of variable- $\delta^{18}\text{O}$ olivines.

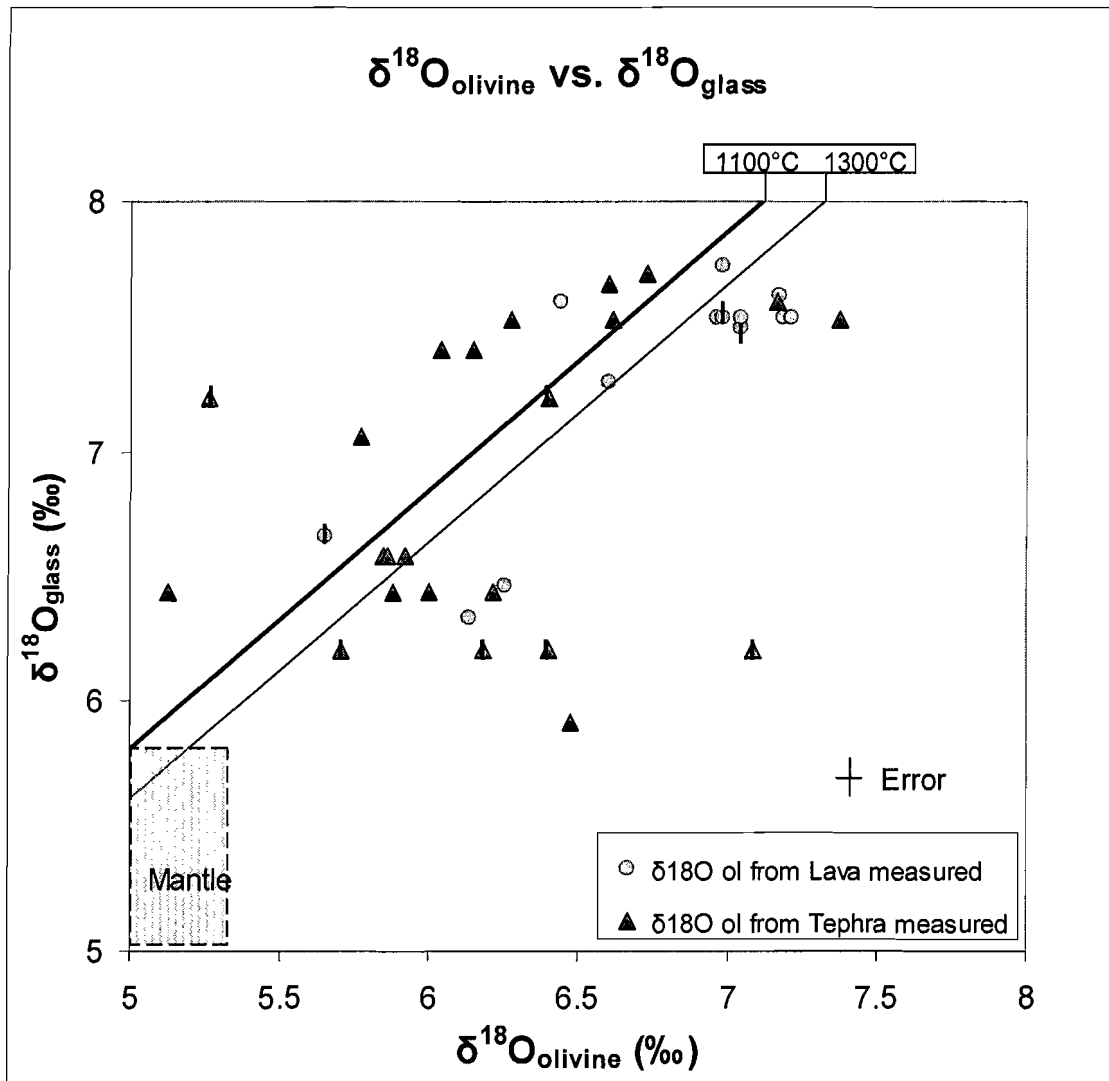
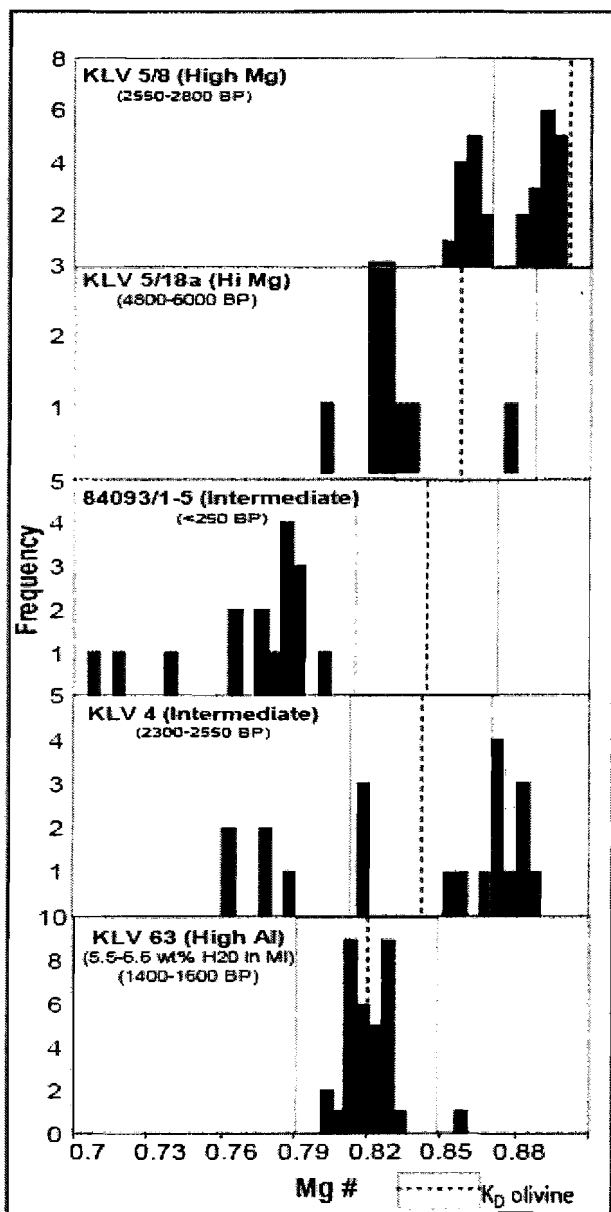


Figure 14. $\delta^{18}\text{O}_{\text{olivine}}$ vs. $\delta^{18}\text{O}_{\text{groundmass}}$ diagram displaying that olivines in a single sample span significant $\delta^{18}\text{O}$ ranges and many are out of equilibrium with the groundmass. Vertical lines on samples indicate individual olivine analyses. Black lines represent calculated groundmass glass-olivine oxygen isotope fractionation using CIPW norm of melt and fractionation factors from Chiba et al. (1989), see text for further discussion.

3.3 Fe-Mg Disequilibrium Between Olivines and Melt

Electron microprobe analysis of olivines and their host groundmass glass, (remelted using the laser) were used to check for compositional Fe-Mg equilibrium



(Figure 15). The wide range of olivine Mg#'s within individual samples of intermediate composition clearly indicate the lack of equilibrium between olivine and its host glass. In addition, normal and reversed zoning from core to rim within individual olivines is present. Both high-Mg and high-Al samples contain olivines that are mostly in Mg-Fe equilibrium with their host glasses, and the olivines show little zoning. Many olivines in the intermediate samples are in Fe-Mg disequilibrium with their groundmass glass.

Figure 15. Olivine-groundmass Mg-Fe equilibrium analyzed by electron microprobe. Equilibrium olivine Mg# values are calculated from measured Mg# of melted groundmass using $K_D=0.3 \pm 0.03$. Grey bars show olivine phenocrysts in equilibrium with the groundmass; black bars are outside the calculated equilibrium range. Olivines in high-Al and high-Mg samples are close to the expected equilibrium with their host glass while intermediate samples have a mixed population of olivines, which were likely brought together by magma mixing and/or cumulate entrainment.

Similar to the approach here, equilibrium K_D calculations were done previously by Kersting and Arculus (1994) with olivine and augite for high-Mg and high-Al basalts. They determined that high-Mg basalts were in equilibrium with Fo_{90} olivine, and thus represent primitive mantle melts, whereas high-Al basalts were consistent with a more evolved liquid. Intermediate compositions were characterized by complex disequilibrium zoning patterns. Khubunaya et al. (2007) reported more complex olivine zoning patterns and wide Fo ranges within many historic lavas, including both high-Al and high-Mg types, and found maximum Fo content in olivine of 91.4, in equilibrium with mantle peridotite. Furthermore, most Mg-rich lavas, including Bulochka, the most Mg-rich basalt in Klyuchevskoy, exhibit bimodal or even trimodal distribution of Fo in cores of olivines with maxima at 91.5-87, 85-83, and <80. The same observations were seen in tephra of this study. Khubunaya et al. (2007) discounted the possibility that most forsteritic olivine found in Klyuchevskoy high-Mg basalts represent xenocrysts from disintegrated mantle peridotitic nodules, but interpreted them as xenocrysts from cumulates of more primitive magmas.

Results of previous studies agree with our new results with the exception that our high-Al samples have olivines that are closer to equilibrium with their host glasses. However, both our and published data support the idea of magma mixing and olivine recycling between endmember high-Al and high-Mg basalts.

3.4 Melt Inclusion Volatile Concentrations

We analyzed olivine-hosted melt inclusions (MI) for their water and CO₂ contents by FTIR and found a wide range of volatile concentrations. **Figure 16** is a graph of all measured water concentrations shown against melt inclusion Mg# and host olivine Fo content.

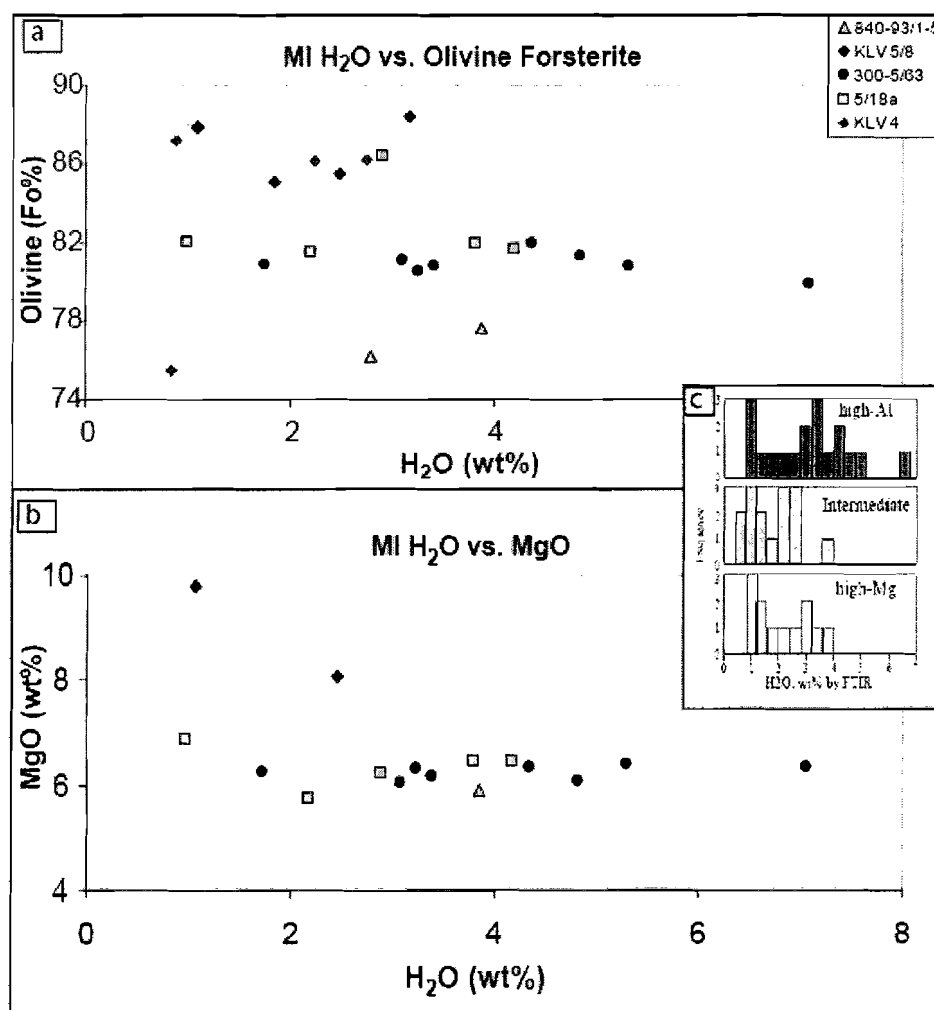


Figure 16. Water concentrations in melt inclusions (MI) vs. compositional parameters (a) forsterite content of host olivine; (b) MgO of melt inclusions (MI) -corrected for post entrapment crystallization and iron loss; (c) Histograms of H₂O measured in melt inclusions for all samples. Analyses of melt inclusions and olivine are given in **Table 2**. Water concentrations were measured using Fourier Transform Infrared Spectroscopy (FTIR). The highest water contents in olivine hosted melt inclusions are in high-Al sample 300-5/63, which has olivines in Fe-Mg equilibrium with the host glass, and has the least chemically diverse, zoned olivines of Fo₈₀. The lowest water concentrations in each sample are likely due to pre-entrapment degassing.

Table 2: Composition of melt inclusions and their host olivines in tephra from Klyuchevskoy volcano									
Major elements and Cl, S, F, were measured by the electron microprobe, trace elements were measured by the ion microprobe									
MI Corrected for Post-entrapment Crystallization (PEC) nd: no data									
<i>Italicized values are analyses in which the probe beam accidentally included both olivine and the melt inclusion glass</i>									
EMPA									
Sample inclusion	840-93/5-18 4a	KLV 4 5A	KLV 4 5B	KLV 4 4B	KLV 4 1	840-93/1-5 3	84093/1-5 4	KLV 5/8 1	KLV 5/8 2
wt%									
SiO ₂	52.27	50.60	50.59	50.63	56.58	<i>49.11</i>	55.45	50.78	50.63
Al ₂ O ₃	17.57	16.07	15.87	15.65	14.58	<i>10.42</i>	16.42	17.46	15.65
Fe ₂ O ₃	1.49	1.33	1.32	1.40	1.60	<i>2.45</i>	1.47	1.36	1.40
FeO	8.43	7.27	7.45	7.92	8.16	<i>12.51</i>	7.50	7.45	7.92
MgO	5.10	7.61	7.80	8.35	4.71	<i>17.09</i>	5.23	7.39	8.35
CaO	8.51	11.78	11.76	10.72	8.05	<i>4.40</i>	8.01	10.63	10.72
Na ₂ O	4.06	3.08	3.04	3.23	3.28	<i>2.20</i>	3.45	2.98	3.23
K ₂ O	0.77	0.63	0.63	0.67	1.16	<i>0.74</i>	0.90	0.57	0.67
TiO ₂	1.06	0.91	0.95	0.87	1.56	<i>0.86</i>	1.10	0.85	0.87
MnO	0.17	0.17	0.09	0.09	0.19	<i>0.24</i>	0.20	0.17	0.09
P ₂ O ₅	0.21	0.19	0.17	0.18	0.25	<i>0.18</i>	0.23	0.16	0.18
S	0.15	0.21	0.20	0.20	0.01	<i>0.01</i>	0.05	0.12	0.20
Cl	0.06	0.07	0.06	0.07	0.05	<i>0.03</i>	0.04	0.05	0.07
F	0.16	0.07	0.07	0.04	nd	<i>0.01</i>	0.08	0.03	0.04
H ₂ O FTIR wt%	3.76	2.24	2.21	2.75	0.84	2.79	3.87	2.49	1.85
CO ₂ FTIR ppm	1067	<50ppm	<50ppm	<50ppm	<50ppm	<50ppm	<50ppm	520	657
Fo Ol host	78.2	86.2	86.2	86.2	76.9	76.2	77.6	85.5	85.1
PEC %	0.0	3.3	5.1	5.4	0.0	0.0	0.0	3.4	5.4

EMPA									
Sample inclusion	KLV 5/8 3	KLV 5/8 4A	KLV 5/8 4B	KLV 5/8 4C	300-5/63 1	300-5/63 2	300-5/63 5	300-5/63 5B	300-5/63 6
wt%									
SiO ₂	50.45	51.57	52.34	nd	53.36	53.16	52.31	51.94	51.24
Al ₂ O ₃	14.99	14.99	15.92	nd	17.29	17.65	17.94	17.99	18.48
Fe ₂ O ₃	1.31	1.24	1.15	nd	1.48	1.45	1.48	1.53	1.61
FeO	6.86	8.20	7.07	nd	7.61	7.46	7.55	7.82	8.22
MgO	9.13	10.40	9.08	nd	5.59	5.49	5.64	6.02	5.67
CaO	12.94	8.86	9.91	nd	9.04	8.81	9.22	8.89	9.08
Na ₂ O	2.59	2.70	2.59	nd	3.39	3.54	3.54	3.57	3.36
K ₂ O	0.42	0.67	0.58	nd	0.66	0.69	0.69	0.75	0.61
TiO ₂	0.82	0.97	0.95	nd	1.12	1.20	1.18	1.12	1.15
MnO	0.12	0.18	0.14	nd	0.14	0.18	0.13	0.11	0.23
P ₂ O ₅	0.12	0.15	0.18	nd	0.20	0.18	0.21	0.24	0.20
S	0.25	0.02	0.02	nd	0.16	0.16	0.16	0.17	0.22
Cl	0.06	0.05	0.05	nd	0.05	0.06	0.05	0.06	0.07
F	0.00	nd	nd	nd	0.02	0.07	0.07	-0.05	0.03
H ₂ O FTIR wt%	1.09	0.40	nd	1.09	1.76	3.40	3.25	3.25	7.09
CO ₂ FTIR ppm	528	<50ppm	<50ppm	<50ppm	<50ppm	<50ppm	887	887	<50ppm
Fo Ol host	88.0	88.3	88.4	nd	80.9	80.8	80.5	80.5	79.9
PEC %	2.4	15.6	7.7	nd	0.8	0.4	0.0	0.0	0.0

EMPA									
Sample inclusion	300-5/63	300-5/63	300-5/63	300-5/63	KLV 5/18a	KLV 5/18a	KLV 5/18a	KLV 5/18a	KLV 5/18a
wt%	7	8	10	11	1	3	4	5	6
SiO ₂	52.88	52.69	53.12	53.51	52.26	53.09	52.41	53.49	50.79
Al ₂ O ₃	17.86	18.42	17.61	17.29	18.50	17.80	18.33	17.44	18.92
Fe ₂ O ₃	1.43	1.43	1.51	1.33	1.43	1.27	1.29	1.00	1.41
FeO	7.32	7.42	7.68	7.44	7.56	8.19	6.84	5.16	7.70
MgO	5.42	5.37	5.72	5.68	5.79	6.29	5.07	5.55	5.77
CaO	9.00	9.01	8.48	9.00	8.88	8.85	10.25	12.38	9.64
Na ₂ O	3.76	3.59	3.66	3.49	2.76	1.80	3.14	3.15	2.42
K ₂ O	0.74	0.64	0.72	0.63	0.99	0.98	1.02	1.04	0.82
TiO ₂	1.16	0.85	1.01	1.03	1.09	1.05	1.00	0.93	1.89
MnO	0.12	0.21	0.17	0.17	0.15	0.14	0.14	0.11	0.16
P ₂ O ₅	0.21	0.22	0.21	0.19	0.23	0.21	0.21	0.25	0.17
S	0.16	0.18	0.15	0.15	0.19	0.19	0.20	0.30	0.15
Cl	0.05	0.06	0.05	0.05	0.08	0.09	0.08	0.13	0.06
F	0.04	-0.09	0.07	0.04	0.09	0.06	0.01	0.03	0.09
H ₂ O FTIR wt%	4.84	3.10	5.32	4.37	3.82	1.00	2.21	2.91	4.20
CO ₂ FTIR ppm	1008	780	1269	<50ppm	1036	703	804	651	1884
Fo Ol host	81.3	81.1	80.8	81.9	82.0	82.0	81.5	86.4	81.7
PEC %	0.0	0.4	0.0	2.9	1.4	8.4	1.6	0.5	2.7

SIMS									
Sample inclusion ppm	840-93/5-18 4a	KLV 4 5a	KLV 4 5b	KLV 4 4b	KLV 4 1	840-93/1-5 3	84093/1-5 4	KLV 5/8 1	KLV 5/8 2
Ba	209	209	220	149	361	nd	377	217	215
U	0.28	0.26	0.23	0.22	0.48	nd	0.43	0.21	0.30
Th	0.34	0.34	0.33	0.30	0.78	nd	0.53	0.27	0.27
K	5463	4806	5266	4377	9602	nd	8027	5616	4728
Cl	nd	nd	nd	nd	nd	nd	429	486	nd
H2O	44454	20484	26711	34481	17950	nd	39365	24924	21187
Nb	1.53	1.46	1.58	1.07	2.78	nd	1.97	1.66	1.32
La	4.89	4.81	4.92	3.35	7.78	nd	6.18	4.09	3.92
Be	0.67	0.34	0.42	0.45	0.84	nd	0.71	0.42	0.52
Ce	12.95	12.46	12.45	9.01	20.41	nd	16.47	10.39	10.80
Sr	255	293	311	217	246	nd	280	285	259
Nd	9.17	9.60	10.28	7.02	15.33	nd	11.39	8.15	8.91
Zr	75	61	65	49	118	nd	85	61	62
B	17.06	10.36	12.80	13.93	19.62	nd	16.18	16.29	15.48
Sm	2.61	3.13	3.04	2.09	4.13	nd	2.98	2.52	2.90
Eu	0.76	0.96	1.24	0.68	1.40	nd	1.12	0.84	0.97
Ti	6007	4115	5338	5344	8352	nd	6367	5473	6459
Dy	2.98	3.18	3.52	2.34	4.77	nd	3.46	2.71	3.23
Y	18.92	17.91	20.02	14.19	28.86	nd	20.70	18.14	20.52
Li	8.14	6.14	6.42	6.98	12.83	nd	10.48	7.07	6.75
Yb	1.85	2.12	2.31	1.52	3.02	nd	2.27	1.93	2.13
F	350	228	295	0.03	0.02	nd	0.03	0.04	0.03
V	247	268	288	226	355	nd	271	265	332
Cr	59	231	215	248	116	nd	69	134	104
Gd	3.13	2.82	3.54	2.76	5.02	nd	3.65	2.23	2.35
Er	1.88	2.35	2.31	1.61	3.47	nd	2.32	1.98	2.51
Hf	2.06	2.26	2.23	1.52	3.31	nd	2.33	1.90	1.79
Pb	1.83	1.54	2.28	1.45	4.04	nd	2.86	3.65	1.89

SIMS									
Sample inclusion ppm	KLV 5/8 3	KLV 5/8 4A	KLV 5/8 4B	KLV 5/8 4C	300-5/63 1	300-5/63 2	300-5/63 5	300-5/63 5B	300-5/63 6
Ba	195	260	215	135	nd	219	202	nd	nd
U	0.18	0.30	0.30	0.24	nd	0.29	0.22	nd	nd
Th	0.27	0.38	0.27	0.22	nd	0.34	0.39	nd	nd
K	4189	6120	5120	3070	nd	6108	5566	nd	nd
Cl	602	nd	nd	nd	nd	574	503	nd	nd
H2O	32370	nd	nd	nd	nd	32875	37867	nd	nd
Nb	1.38	1.68	1.50	0.92	nd	1.93	1.83	nd	nd
La	3.81	4.87	4.12	2.84	nd	5.02	4.82	nd	nd
Be	0.39	nd	nd	nd	nd	0.60	0.59	nd	nd
Ce	10.30	13.66	11.08	8.12	nd	12.90	12.67	nd	nd
Sr	249	271	248	212	nd	285	270	nd	nd
Nd	8.73	9.63	8.54	6.35	nd	9.82	9.03	nd	nd
Zr	60	70	63	43	nd	79	78	nd	nd
B	11.96	nd	nd	nd	nd	18.69	15.07	nd	nd
Sm	2.83	2.61	2.78	1.73	nd	2.96	2.72	nd	nd
Eu	0.89	0.86	0.90	0.75	nd	0.87	0.88	nd	nd
Ti	5613	nd	nd	nd	nd	5910	5905	nd	nd
Dy	3.14	3.29	2.92	2.35	nd	3.13	2.99	nd	nd
Y	20.14	20.05	17.46	14.32	nd	19.07	17.94	nd	nd
Li	5.38	nd	nd	nd	nd	7.73	7.17	nd	nd
Yb	2.25	2.37	1.76	1.81	nd	1.99	2.06	nd	nd
F	0.03	nd	nd	nd	nd	0.03	0.03	nd	nd
V	305	278	265	263	nd	255	239	nd	nd
Cr	204	100	136	255	nd	95	74	nd	nd
Gd	2.30	3.02	2.78	1.97	nd	3.19	2.74	nd	nd
Er	2.12	2.46	2.02	1.74	nd	2.06	1.94	nd	nd
Hf	1.91	2.01	1.81	1.50	nd	2.20	2.03	nd	nd
Pb	1.38	2.83	1.91	1.35	nd	2.17	2.02	nd	nd

SIMS									
Sample inclusion	300-5/63	300-5/63	300-5/63	300-5/63	KLV	KLV	KLV	KLV	KLV
ppm	7	8	10	11	5/18a	5/18a	5/18a	5/18a	5/18a
					1	3	4	5	6
Ba	205	203	nd	nd	nd	nd	nd	nd	nd
U	0.26	0.28	nd	nd	nd	nd	nd	nd	nd
Th	0.37	0.38	nd	nd	nd	nd	nd	nd	nd
K	5740	5559	nd	nd	nd	nd	nd	nd	nd
Cl	491	575	nd	nd	nd	nd	nd	nd	nd
H ₂ O	32355	34128	nd	nd	nd	nd	nd	nd	nd
Nb	1.95	2.18	nd	nd	nd	nd	nd	nd	nd
La	5.06	5.35	nd	nd	nd	nd	nd	nd	nd
Be	0.62	0.65	nd	nd	nd	nd	nd	nd	nd
Ce	13.09	12.96	nd	nd	nd	nd	nd	nd	nd
Sr	276	277	nd	nd	nd	nd	nd	nd	nd
Nd	9.59	9.74	nd	nd	nd	nd	nd	nd	nd
Zr	80	84	nd	nd	nd	nd	nd	nd	nd
B	15.79	16.76	nd	nd	nd	nd	nd	nd	nd
Sm	2.73	2.41	nd	nd	nd	nd	nd	nd	nd
Eu	0.90	0.87	nd	nd	nd	nd	nd	nd	nd
Ti	6134	6339	nd	nd	nd	nd	nd	nd	nd
Dy	2.95	3.01	nd	nd	nd	nd	nd	nd	nd
Y	19.38	20.73	nd	nd	nd	nd	nd	nd	nd
Li	7.09	7.97	nd	nd	nd	nd	nd	nd	nd
Yb	1.85	2.06	nd	nd	nd	nd	nd	nd	nd
F	0.02	0.03	nd	nd	nd	nd	nd	nd	nd
V	243	259	nd	nd	nd	nd	nd	nd	nd
Cr	87	59	nd	nd	nd	nd	nd	nd	nd
Gd	2.65	2.81	nd	nd	nd	nd	nd	nd	nd
Er	2.12	1.98	nd	nd	nd	nd	nd	nd	nd
Hf	2.35	2.20	nd	nd	nd	nd	nd	nd	nd
Pb	1.71	2.01	nd	nd	nd	nd	nd	nd	nd

The highest H₂O values of 7.1 and 5.3 wt% were found in Fo₈₀ olivine in the most Al-rich sample (300-5/63) (Table 2; Figure 16). The highest CO₂ concentration of 1933 ppm was found in sample KLV 5/18a, with a corresponding H₂O value of 4.2 wt% (Figure 17). The lowest values were ~1 wt% H₂O, and the majority of samples contained CO₂ at levels below the detection limit of 50 ppm. This wide range of CO₂ and H₂O values is likely caused by degassing and olivine crystallization during magma ascent. The highest volatile concentrations therefore are our best estimate of original magmatic concentrations. Calculation of pressures associated with these volatile contents (using the VolatileCalc program; Newman and Lowenstern 2002) indicate a maximum depth of crystallization of ~17 km (5 kbar) for melts with 1993 ppm CO₂ and 4.2 wt% H₂O.

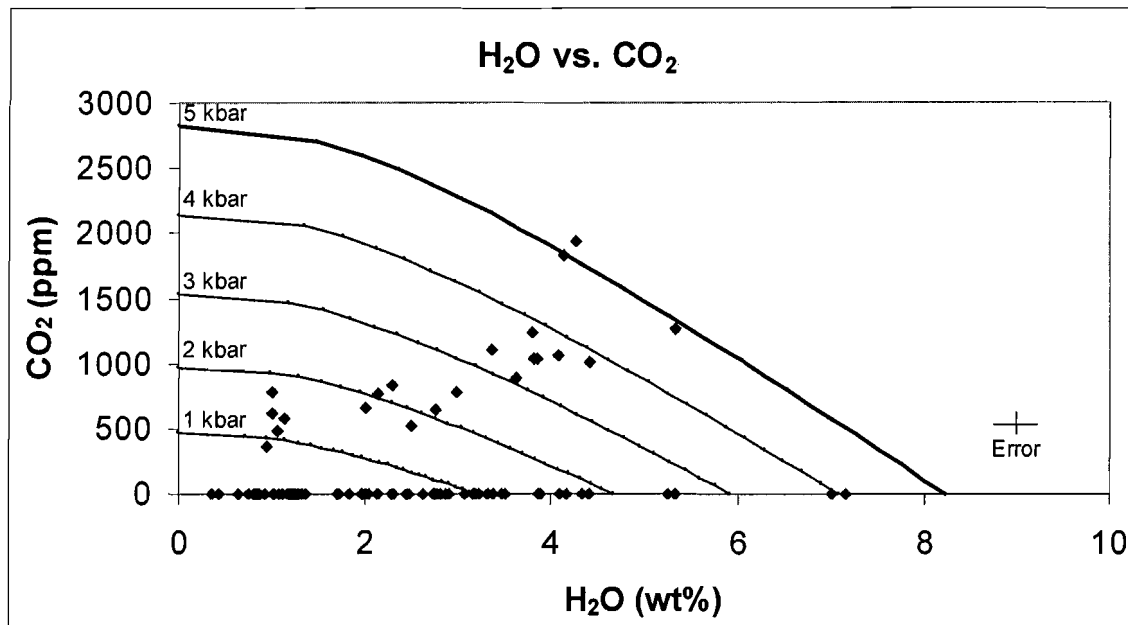


Figure 17. H₂O vs. CO₂ concentrations in melt inclusions. A wide range of volatile concentrations are present and correspond to partial pressures of 0-5 kbars, as indicated by the dark curved lines. The maximum CO₂ concentration (1933 ppm with 4.2 wt% H₂O) corresponds to ~5 kbars partial pressure or a maximum depth of crystallization of ~17 km.

We have obtained what we believe to be the highest reported water concentrations known for Klyuchevskoy and one of the highest known for any arc basalt. Other arc basalts such as those from Cerro Negro (Nicaragua), the Marianas, and the Central Mexican Volcanic Belt range up to 6 wt% H₂O (Wallace 2005). The high-Mg andesites of Mt. Shasta are even more hydrous with 8-10 wt% H₂O (Anderson, 1973). We attribute our discovery of such high H₂O values to our emphasis on tephra samples that rapidly quenched and thus preserved the highest water concentrations. Previous researchers who studied natural or reheated melt inclusions from olivines in lavas from Klyuchevskoy (e.g. Mironov et al. 2001; Portnyagin et al. 2007a,b) obtained lower concentrations of water (0-4 wt%) and no detectable CO₂.

3.5 Trace Element Variations in Melt Inclusions

Overall, trace element concentrations in melt inclusions from both high-Mg and high-Al basalts (**Table 2**), when normalized to depleted mantle values (e.g. Sun and McDonough 1989), exhibit a pattern typical of arc basalts (**Figure 18**) suggesting that to a first order they are similar to each other (Gill 1981).

Major element crystallization modeling (using the MELTS program) involving fractionation of olivine and clinopyroxene from our endmember high-Mg basalt (Table 1), shows that 20% fractional crystallization is required to yield high-Al basalt. This 20% fractional crystallization would produce evolved melts in equilibrium with Fo₈₀ olivine if crystallization started from a high-Mg basalt parent with 9 wt% MgO that initially crystallized Fo₈₈ olivine. This 20% fractionation can

be used to recalculate incompatible trace element concentrations in the high-Al basalts to compare primitive melt compositions for both basalt types. After performing this procedure, closer examination of trace element data for melt inclusions shows that there are still systematic (although subtle for some

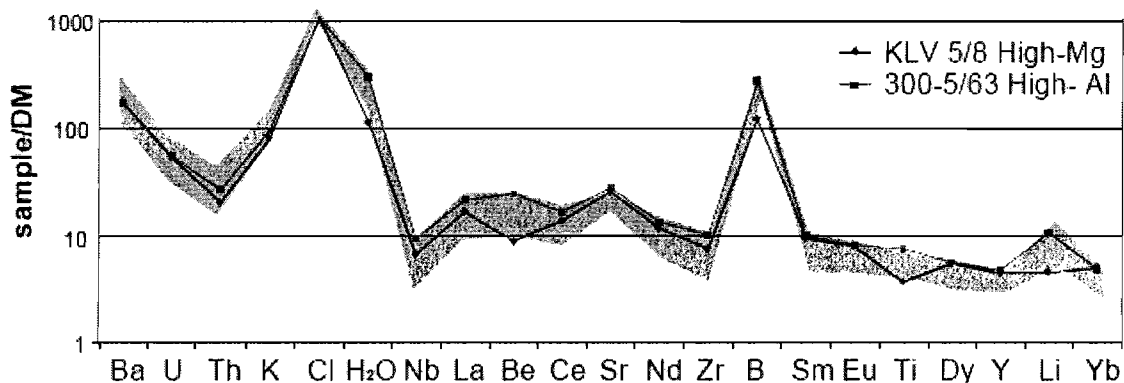


Figure 18. Spider diagram of trace elements in olivine-hosted melt inclusions within tephra from Klyuchevskoy volcano (See Table 2 for analyses). (a) average composition of high-Mg (KLV 5/8) and high-Al (300-5/63) melt inclusions normalized to a depleted mantle that emphasizes the island-arc, zigzag pattern with peaks in fluid-mobile and depressions in fluid immobile elements.

elements) differences in Ba, U, Cl, H₂O, Be, Ce, Sr, Nd, B, Sm, Eu, Dy, Y, Li, and Yb between high-Al and high-Mg end members even when accounting for the effects of fractional crystallization. **Figure 19** illustrates this, with markedly higher concentrations of H₂O, Be, B, and Li in high-Al samples compared to high-Mg. The ⁸⁷Sr/⁸⁶Sr values of high-Al and high-Mg samples are also different, with 0.70366 in high-Al and 0.70355 in high-Mg samples using data from Dorendorf et al. (2000). Even excluding the oxygen isotope evidence described above, the 20% fractional crystallization cannot account for these discrepancies in elemental

concentrations and Sr isotopic ratios between high-Al and high-Mg compositions

(Figure 19).

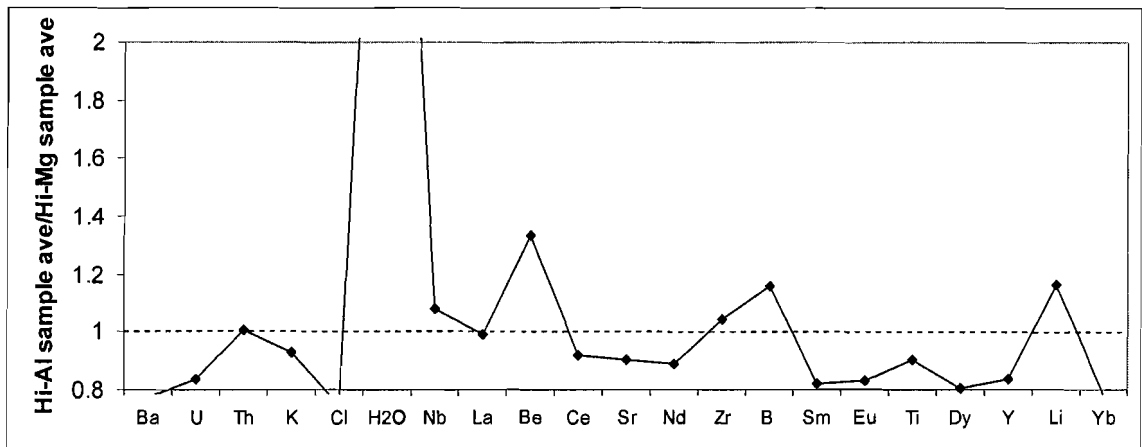


Figure 19. Trace element comparison of high-Al to high-Mg samples at Fo_{88} . Average composition of four high-Al melt inclusions in sample 300-5/63 are normalized to three high-Mg melt inclusions in sample KLV 5/8, with the high-Al sample 300-5/63 calculated back to Fo_{88} , the same Fo as in KLV 5/8, see Tables 2 and Appendix B for analyses. Elements falling around 1 are found in similar concentrations for both high-Al and high-Mg samples. Elements falling below 1 or above 1 are depleted or enriched in the high-Al sample respectively compared to the high-Mg sample.

CHAPTER IV

DISCUSSION

We have examined Klyuchevskoy's magmatic history through a variety of techniques, and we attempt below to interpret this information to attain a better understanding of the sources and processes involved in magma evolution for this giant arc volcano. In particular we evaluate processes that may have caused the observed high $\delta^{18}\text{O}$ values and high H_2O contents in Klyuchevskoy magmas. We also comment on the complexities of crystal-melt relationships.

4.1 Olivine Recycling Processes Under Klyuchevskoy

Oxygen isotope disequilibrium of up to 1‰ from estimated olivine-host glass equilibrium values provides the first evidence for olivine recycling within Klyuchevskoy through mechanisms of magma mixing and/or cumulate addition. Fe-Mg disequilibria between olivines and their host glasses provides further support for olivine recycling in some samples (mainly intermediate compositions).

The olivine-melt isotopic and chemical disequilibria in high- $\delta^{18}\text{O}$ Klyuchevskoy magmas are similar in magnitude to the low- $\delta^{18}\text{O}$ disequilibria discovered in the Laki eruption of Iceland (Bindeman et al. 2006). By comparison with Laki, Fe-Mg and $\delta^{18}\text{O}$ equilibration of olivine by diffusion happens on timescales of weeks and hundreds of years, respectively.

4.2 Peridotite vs. Pyroxenite Source and Crustal Assimilation Models

Determination of the source of Klyuchevskoy's magma is a necessary component for understanding how this magma obtains high $\delta^{18}\text{O}$ values. Three main components are considered: 1) a secondary pyroxenite derived from slab-derived melt reacting with the mantle wedge to produce olivine-free pyroxenite; 2) an amphibolite present in the lower crustal roots, emplaced by accretion of Cretaceous mafic to ultra-mafic material (e.g. Konstantinovskaia, 2001); and 3) older mantle wedge material that was extensively hydrated from ~46-5 m.y.a. when the mantle beneath Klyuchevskoy was part of the forearc region (See Figure 2-tectonic summary).

The $\delta^{18}\text{O}$ values of mantle pyroxenites formed in the manner described above are likely to vary from place to place but could be high due to subduction of the upper portions of the oceanic crust altered at low temperature by sea water (Muehlenbachs, 1986; Staudigel et al. 1995). Lower to middle crustal amphibolite sources can potentially explain the high water contents and compositional range of Klyuchevskoy magmas through assimilation of the material. A peridotite source, on the other hand, is much more widespread as it is found throughout the mantle wedge. However, normal mantle peridotite is not enriched in $\delta^{18}\text{O}$ and to produce a range of $\delta^{18}\text{O}$ -enriched signatures, would have to be somewhat altered by high- $\delta^{18}\text{O}$ fluid or melt fluxing, such as likely occurred when this region was part of the forearc.

Using Sobolev et al.'s (2007) compilation of trace element concentrations in olivines, we plot Klyuchevskoy olivines on their discriminant diagrams (**Figure 20**), which demonstrate that pyroxenite partial melts are higher in Ni, but poorer in Mn than peridotite-derived melts. Different magmas from plume and MORB environments were shown to plot between these two end members. We observe that the Klyuchevskoy olivines plot solidly within the peridotite field, which precludes their derivation from an olivine-free pyroxenite mantle.

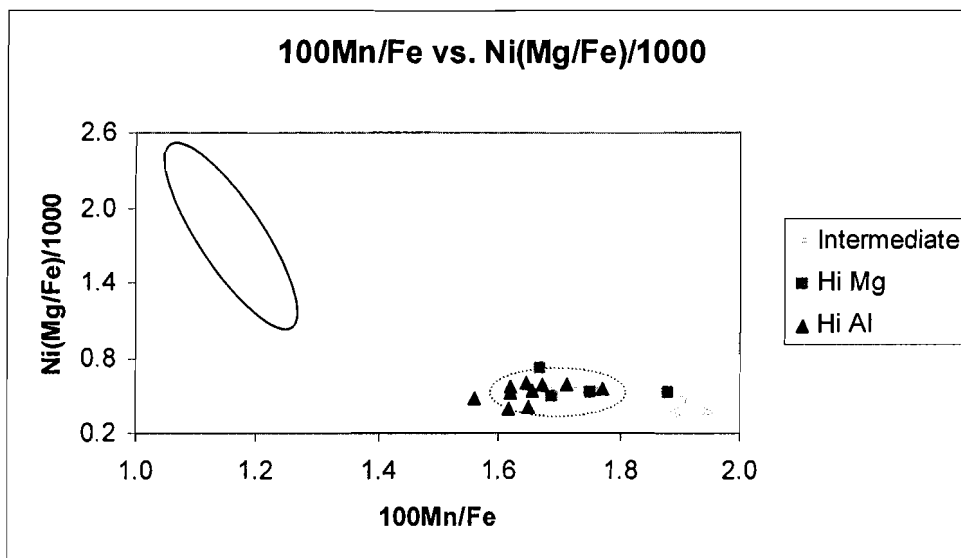


Figure 20. Trace element concentration ratios in olivines plotted on peridotite-pyroxenite discrimination diagram (Sobolev et al. 2007). The solid oval indicates a pyroxenite source while the dashed oval indicates a peridotite source. Data from this study clearly falls in the peridotite source field.

Furthermore, we notice that Klyuchevskoy basalts are characterized by low Nb concentrations (**Figure 18**), which suggests melting of a relatively depleted mantle wedge (Sun and McDonough 1989).

Next, we examine the possibility that a melt generated primarily from mantle peridotite could assimilate enough amphibolite from the high- $\delta^{18}\text{O}$ lower crust to impart a high- $\delta^{18}\text{O}$ signature while still retaining a peridotite source. We

examine this through two models using a typical 2 wt% H₂O basalt (e.g. Churikova et al. 2001) with 48 wt% SiO₂ and mixing it with variable amounts of amphibolite melt containing 55 or 68 wt% SiO₂; 10, 15, or 20‰ δ¹⁸O values; and 2, 3, or 4 wt% H₂O. Contamination of mantle-derived magma by crustal amphibolite could happen by two differing methods: 1) bulk digestion of amphibolite by this primary basaltic magma or 2) partial melting of the amphibolite and mixing of the partial melt with the primary basaltic magma. For partial melt, our calculations assume 33% partial melting of amphibolite, leading to the dacitic partial melt containing all of the water present in its source. We use three diagrams to explore these possibilities. The mass balance relationships were calculated using the following relationship: $\delta^{18}\text{O}_{\text{amphibolite}} \cdot (1-f) + f \cdot \delta^{18}\text{O}_{\text{magma}} = \delta^{18}\text{O}_{\text{final magma}}$; where f is the fraction of the primary basalt component. First we start with a δ¹⁸O-SiO₂ diagram (**Figure 21**) and establish that only a 10-15‰, 68 wt% SiO₂ amphibolite partial melt would satisfy observed Klyuchevskoy values, but would require the addition of 20-30% of such a component. Next, we examine a δ¹⁸O-H₂O diagram using our best fit of a 10-15‰ partial melt of amphibolite, with initial water concentrations of 2, 3, and 4 wt% (**Figure 22**). This amphibolite if partially melted by 33% would result in a product containing upwards of 8, 10, and 12 wt% H₂O (e.g. 4% initial H₂O in amphibolite translates into 12 wt% H₂O in a 33% partial melt). No one model adequately fulfills observed δ¹⁸O and water concentrations seen at Klyuchevskoy. Finally, when we plot a SiO₂-H₂O diagram (**Figure 23**) no single model can account for the

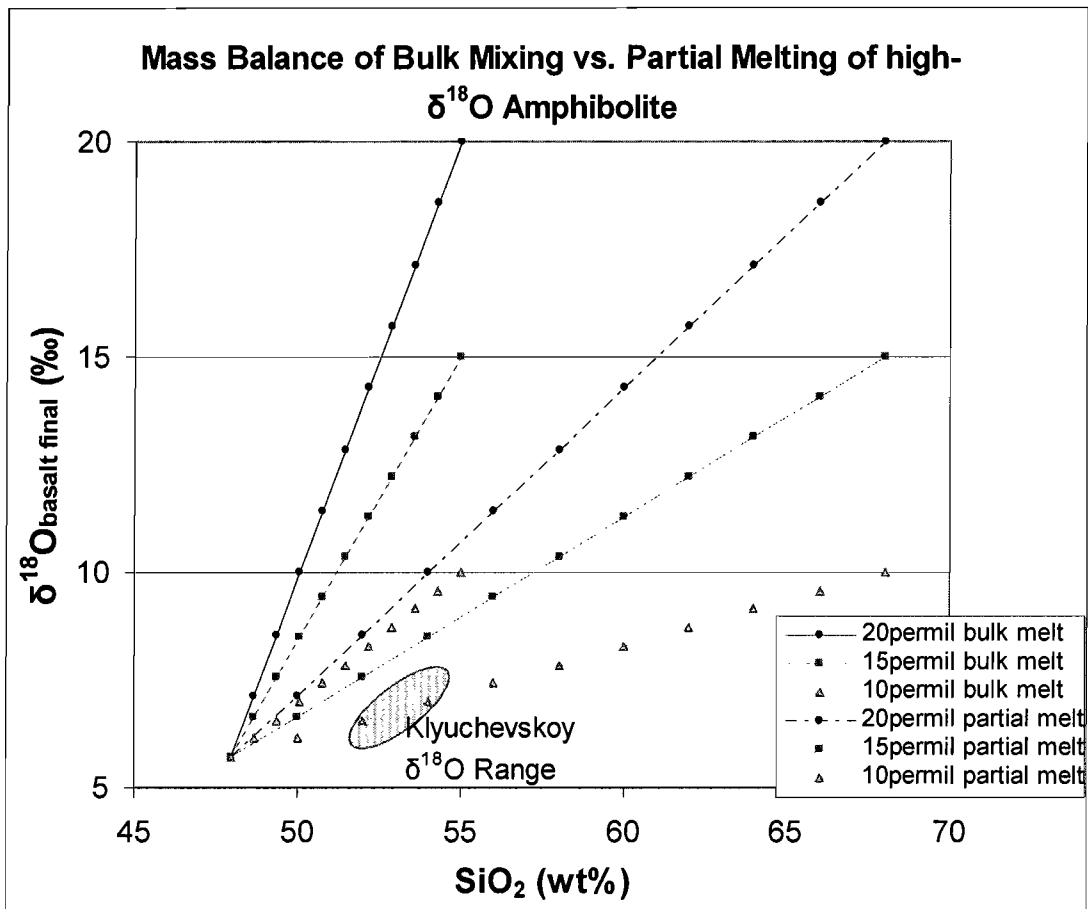


Figure 21. $\delta^{18}\text{O}$ - SiO_2 diagram. This diagram examines models for assimilation of amphibolite through 1) bulk melting and 2) partial melting; and mixing with the mantle wedge. All models start w/ 0% assimilation and each point on the model lines represents a 10% increment of assimilated material until the final point on the model lines represents 100% assimilated material. To fit observed Klyuchevskoy trends, 20-30% assimilation of a 10-15‰, 68 wt% SiO_2 partial melt will be required.

compositional and H_2O range. Instead a partial melt with a wide range of H_2O concentrations and a maximum H_2O value of >12 wt% H_2O would be required to fit Klyuchevskoy data at a fraction of 20-30%.

It is clear that no one amphibolite mixing model can account for the $\delta^{18}\text{O}$ - SiO_2 - H_2O values observed at Klyuchevskoy. We also notice that the current mass balance calculations have no heat balance. Assimilation of colder crustal material results in a temperature decrease and magma crystallization of

accumulates of comparable magnitude (e.g. DePaolo 1981; Spera and Bohrsen 2002). This assimilation-fractional crystallization (AFC) process would result in

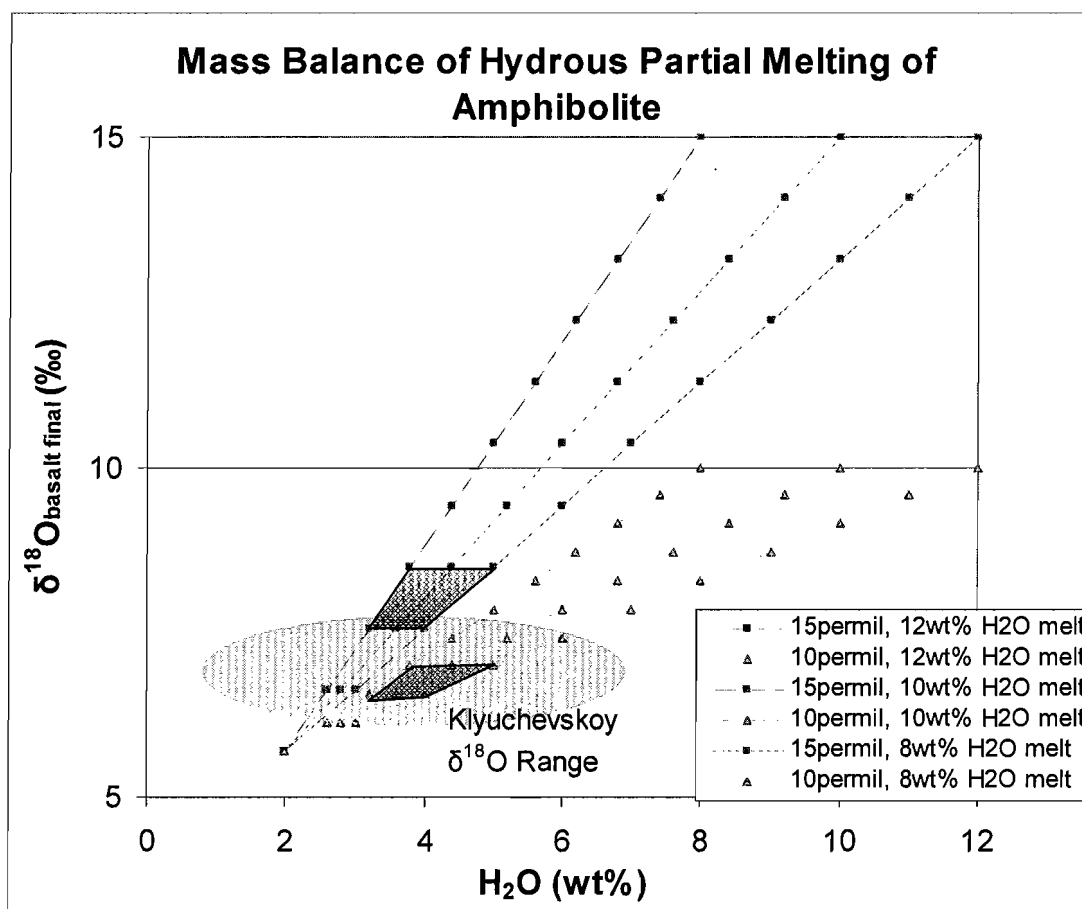


Figure 22. $\delta^{18}\text{O}$ -H₂O diagram. This diagram examines models for H₂O contribution assimilation of a partial melt of amphibolite could provide assuming assimilant water concentrations of 8, 10, and 12 wt%. Using our best fit of 20-30% assimilation (polygon shaded in dark grey) of a 10-15‰ partial amphibole/pyroxenite melt, it is clear the wide range of melts with differing H₂O concentrations and $\delta^{18}\text{O}$ values would be need to explain the observed $\delta^{18}\text{O}$ and H₂O ranges found at Klyuchevskoy.

compositional evolution of the melt to more siliceous compositions than predicted in the models, and even farther outside the compositional range of Klyuchevskoy Volcano. As no single amphibolite assimilation model can suitably account for observed Klyuchevskoy $\delta^{18}\text{O}$ -SiO₂-H₂O values, we accept the likelihood of a strictly peridotite source.

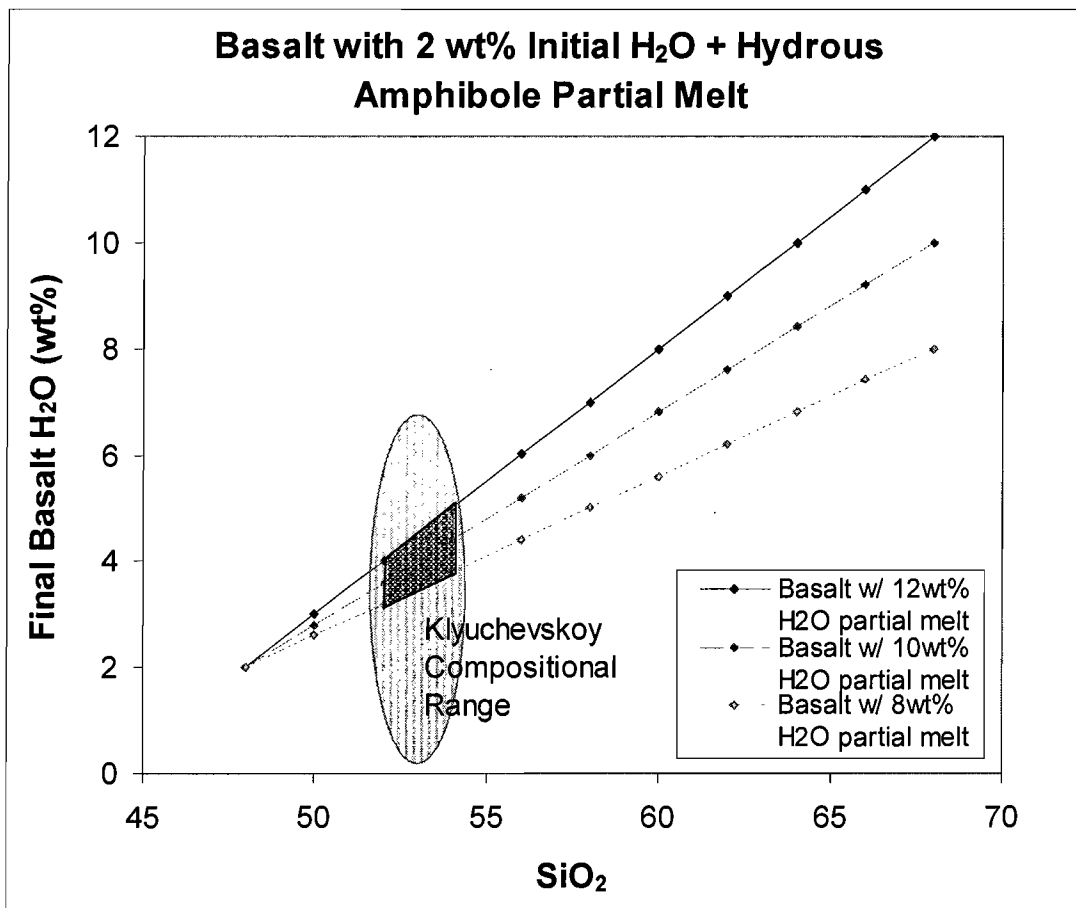


Figure 23. SiO₂-H₂O diagram. Three models of a basalt-amphibolite partial melt with 8, 10, and 12 wt% H₂O over a SiO₂ range of 48-68 wt% are presented. The only model that can account for the compositional and H₂O range of Klyuchevskoy is a partial melt with 12wt% H₂O at a fraction of 20-30%.

4.3 Evidence for High H₂O Primary Melts Under Klyuchevskoy

We have found evidence for a range of H₂O contents of <1.0-7.1 wt%, with the majority of values between 2 and 5 wt%. We take our maximum water concentration of 7.1 wt% in a melt inclusion in Fo₈₀ olivine to estimate the maximum water concentration in the source of these magmas. MELTS modeling of fractional crystallization of an olivine-clinopyroxene assemblage requires 20% fractional crystallization from a parental melt in equilibrium with Fo₈₈ and 25%

from a parental melt in equilibrium with Fo₉₀ olivine. Using these proportions, we obtain the maximum of 5.3 wt% H₂O in the primary basaltic magma of Klyuchevskoy, over 2% higher than originally predicted by Portnyagin et al. (2007b).

The high H₂O contents at Klyuchevskoy may explain the high $\delta^{18}\text{O}$ values and high magma production rates. These characteristics may be related to subduction and fluxing of fluids from the upper portion of the Hawaii-Emperor Seamount Chain (high- $\delta^{18}\text{O}$ due to low temperature reaction with seawater) under Central Kamchatka Depression as was suggested by previous researchers (Kersting and Arculus 1994; Dorendorf et al. 2000). However, the presence of variably high- $\delta^{18}\text{O}$ values ranging across arc, rather than just in the Klyuchevskoy area suggests that the Hawaii-Emperor Seamount Chain alone is not responsible for the high- $\delta^{18}\text{O}$ values. Fluxing of high- $\delta^{18}\text{O}$ fluids from the subducting Hawaii-Emperor Seamount Chain in the Klyuchevskoy area could be the reason that high- $\delta^{18}\text{O}$ values peak in the Klyuchevskoy Group area. However, another widespread high- $\delta^{18}\text{O}$ source, such as high- $\delta^{18}\text{O}$ serpentized mantle in what was once the forearc, is likely a possible contributor to the across arc $\delta^{18}\text{O}$ enrichment and is discussed in section 4.5.

4.4 Origin of High- $\delta^{18}\text{O}$ Peridotite Source Klyuchevskoy Magmas

Oxygen is a major element in rocks and magmas and its isotopic values therefore provide robust constraints on mass balances required to achieve

significant (i.e. 1-2 ‰) isotopic changes. We have shown that simple fractionation of a parental high-Mg basalt to form a high-Al basalt, a common scenario in many interpretations of arc petrogenesis at Klyuchevskoy and other volcanoes worldwide (e.g. Kersting and Arculus 1994), cannot account for the 2‰ enrichment of $\delta^{18}\text{O}$ values, contrasting Sr isotopic ratios, and details of trace element distribution. Likewise, assimilation processes are unlikely to be the cause of Klyuchevskoy's hydrous high- $\delta^{18}\text{O}$ magmas because assimilation of amphibolite cannot account for observed Klyuchevskoy $\delta^{18}\text{O}$ - SiO_2 - H_2O values.

We computed a simple mass balance for the amount of slab-derived H_2O -rich material added to the normal mantle wedge using various plausible $\delta^{18}\text{O}$ values of the slab-derived fluid or melt (**Figure 24**). The maximum $\delta^{18}\text{O}$ in H_2O -rich fluid or silicate melt that could be inherited from the upper portion of the subducted slab in front of Kamchatka is 8-10‰ for altered basalts (Bailey, 1996) and 10-20‰ for sediments (Bindeman et al. 2004). As can be seen from the diagram, because water has more oxygen on a molar basis than silicate melt, fluxing with solute-free water is more efficient than fluxing with melt.

If the proportion of H_2O -rich fluid added to the mantle wedge to generate basaltic magma is 0.8-2.1 wt% (Churikova et al. 2001), then the $\delta^{18}\text{O}$ value of the fluid would have to be exceedingly high. Only marine-precipitated carbonate with $\delta^{18}\text{O}$ values as high as +25‰ would be capable of explaining such high $\delta^{18}\text{O}$ values at Klyuchevskoy. However, no significant carbonate is found in sediments offshore from Kamchatka (e.g. Bailey 1996) suggesting that a high- $\delta^{18}\text{O}$ marine-

precipitated component is absent in front of the Kamchatka arc. Even if we take the highest water concentration of 7.1 wt% water and translate it into 5.7 wt% water in primary mantle-equilibrated magma, given our mass balance calculation (**Figure 24**) the high- $\delta^{18}\text{O}$ values of olivines of up to 7.2‰, would require a 20‰ water-rich fluid. While these values are possible in subduction zones, we consider them extreme, and not appropriate for the majority of the subducted sediments beneath Kamchatka.

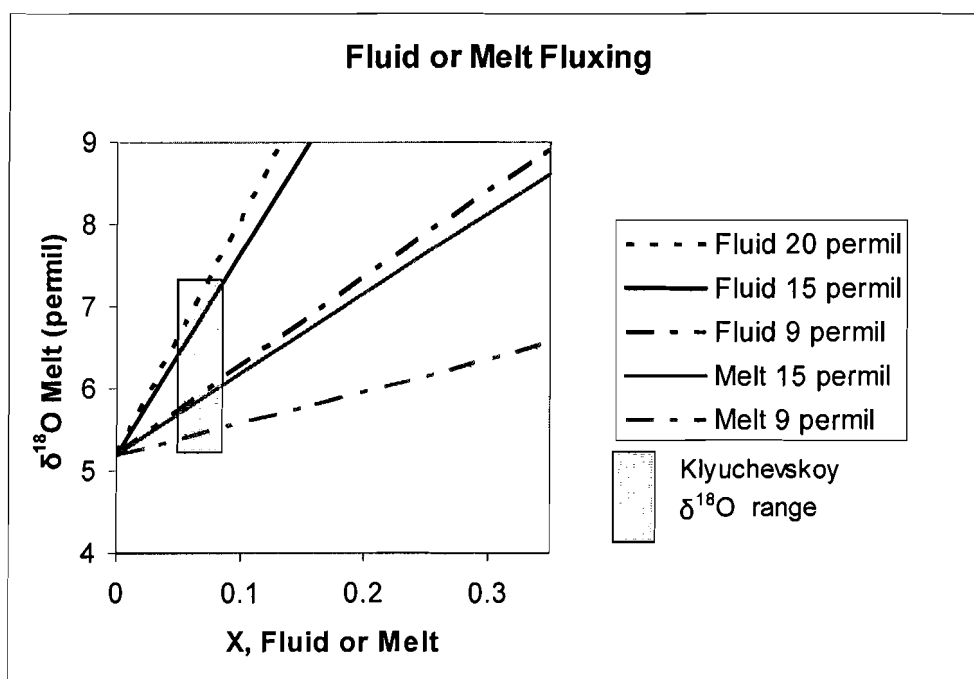


Figure 24. Mass balance calculation of high- $\delta^{18}\text{O}$ fluid or melt flux melting of normal $\delta^{18}\text{O}$ peridotite. Differing proportions of water-rich and silicate-rich components are proposed to be added to the normal mantle wedge for differing fluid or melt $\delta^{18}\text{O}$ values. Calculations for the fluid component use the same equation presented in section 4.2 for melt mass balance with the addition of the oxygen proportion for fluid to rock (0.89/0.5) resulting in the equation: $(0.89/0.5) * \delta^{18}\text{O}_{\text{fluid}} * (1-f) + f * \delta^{18}\text{O}_{\text{magma}} = \delta^{18}\text{O}_{\text{final magma}}$. Notice that in order to make Klyuchevskoy high- $\delta^{18}\text{O}$ olivines in a single stage flux melting very high $\delta^{18}\text{O}$ values of fluid are required.

Instead of excessively high $\delta^{18}\text{O}$ H_2O -rich fluids as required above, Dorendorf et al. (2000) proposed a model of time-integrated fluid addition without melting, in which peridotite is progressively enriched in ^{18}O by multiple episodes of fluid addition. While such a model is theoretically possible, it should yield unusually high fluid-mobile element signatures such as high Ba/La. Our ion microprobe analyses of melt inclusions within olivines do not show such features in Klyuchevskoy magmas (**Table 2**). Furthermore, for our measured H_2O contents, the Dorendorf model would require that H_2O would have to be continuously lost from the wedge after each episode of fluid addition, but how this occurs or how so much H_2O is fluxed through the wedge without causing melting is not specified.

We noted above that fluxing with moderately high- $\delta^{18}\text{O}$ hydrous melt is somewhat less efficient in terms of mass balance (we would need more mass of melt than fluid), but it is more permissive with respect to major and trace elements provided that the final source material for Klyuchevskoy magmas retains a peridotite signature in terms of Mg/Fe, Ni, and Mn (**Figure 20**). For example, a slab-melt component, if variably added to the peridotitic wedge, could explain major and trace element differences between volcanoes (Portnyagin et al. 2007a,b). Because of the large proportion of peridotite in these mixing models, no clear adakitic signatures would be present except in the northernmost, slab edge volcanoes such as Shiveluch, Zarechny and Kharchinsky (Bindeman et al. 2005) whose source would be primarily slab melt. It is, however, expected from mass balance, that a slab-derived dacitic melt

component is moderately high in $\delta^{18}\text{O}$ (6-9‰), as these are the values for the upper portions of the altered oceanic crust. Only in areas of active sediment melting such as in Setouchi, Japan, could melts significantly higher in $\delta^{18}\text{O}$ (Bindeman et al. 2005) be due to extremely enriched $\delta^{18}\text{O}$ values of the original sediment.

4.5. Inheritance of High- $\delta^{18}\text{O}$ Signature from Prior Enrichment

A high- $\delta^{18}\text{O}$, water-rich subduction-derived component that reaches its extreme beneath Klyuchevskoy, is variably present in other volcanoes of the Central Kamchatka Depression (Portnyagin et al. 2007a) and throughout Kamchatka (Bindeman et al. 2004). It is particularly characteristic for back-arc volcanoes to the south such as Opala, Koryaksky, Kizimen, and overall $\delta^{18}\text{O}$ value of mafic volcanics increase across the arc. In order to explain this feature, we suggest that magmas in the CKD tap a higher- $\delta^{18}\text{O}$ mantle source and that mantle source may represent serpentinized peridotite fluxed for millions of years by high- $\delta^{18}\text{O}$ fluids.

As discussed in chapter 1, the accretion of eastern peninsulas onto Kamchatka several million years ago (Konstantinovskaya et al. 2001) stalled subduction causing the subduction trench to roll back to its present position (**Figure 2**). This subduction jump exposed a previously fluxed forearc region in the mantle wedge to rising basaltic magmas in the present subduction configuration. The time-integrated fluid fluxing of the previously forearc region

has also led to higher concentrations of Li, Be and B, as well as water, while maintaining the peridotitic source. In this subduction jump model the high- $\delta^{18}\text{O}$ signature is characteristic of the Kamchatkan back arc volcanoes, but the level of ^{18}O enrichment is expected to be variable along the arc. The stronger-fluxed and serpentinized areas, previously affected by additional high- $\delta^{18}\text{O}$ fluid fluxes from the subducting Hawaii Emperor Chain (e.g. Dorendorf et al. 2000) has led to ^{18}O -rich and hydrous mantle under the present Central Kamchatka depression, and Klyuchevskoy in particular.

In the proposed model (**Figure 25**) a variably-high ^{18}O signature is acquired in the upper mantle, just below the Moho where basaltic liquids may pond. Ascending hydrous mafic melts generated by flux melting of the underlying mantle wedge are capable of digesting significant volumes of very shallow, high- $\delta^{18}\text{O}$ previously-hydrated peridotitic mantle. Unlike the classic MASH process under island arcs where basaltic magmas assimilate basaltic arc roots (e.g. Hildreth and Moorbath, 1988; Ducea and Barton 2007) to explain high- $\delta^{18}\text{O}$ signature of more siliceous volcanics, we propose an analogous process that happened to peridotite. A complication to this hypothesis is that thermal models for the mantle wedge (Manea and Manea 2006) suggest temperatures in the uppermost mantle that are too high for serpentine and probably chlorite (Grove et al. 2006). Therefore the previously hydrated forearc would have been heated after the slab jump, driving off H_2O but retaining high $\delta^{18}\text{O}$.

The isotopic and chemical differences that we observe between high-Al and high-Mg basalts fit sensibly into the proposed model. High-Al, higher- $\delta^{18}\text{O}$, higher $^{87}\text{Sr}/^{86}\text{Sr}$ basalts involve a larger component from the older previously hydrated peridotitic environment, whereas the high-Mg basalts contain less of this component. Both melts erupt coevally and mix to a variable degrees upon ascent. This model provides a mechanistic interpretation for the complex olivine recycling processes that we documented. Olivine recycling happens in upper crustal magma chambers and also upon ascent of different magmas. Furthermore, high magma production rates at Klyuchevskoy and the surrounding group volcanoes may be explained by fluid fluxing from the subducting Hawaii-Emperor Seamount Chain.

4.6. Comparison with Mt Shasta: A High- $\delta^{18}\text{O}$ H₂O-rich Volcano

Comparison with Mt Shasta is warranted because in both places high magma production rates are coupled with high- $\delta^{18}\text{O}$ signatures and high H₂O contents (Grove et al. 2002; 2006). A key to understanding the cause of high- $\delta^{18}\text{O}$ magmas at Klyuchevskoy can be found by examining anomalies present at both subduction zones. For Klyuchevskoy, the subduction of the Hawaii-Emperor chain, in addition to previously serpentized mantle, could provide the high- $\delta^{18}\text{O}$ values and high H₂O contents. For Mt. Shasta, however, it is the presence of the subducting Blanco fracture zone that could contribute to enhanced permeability of sea water within the oceanic lithosphere before

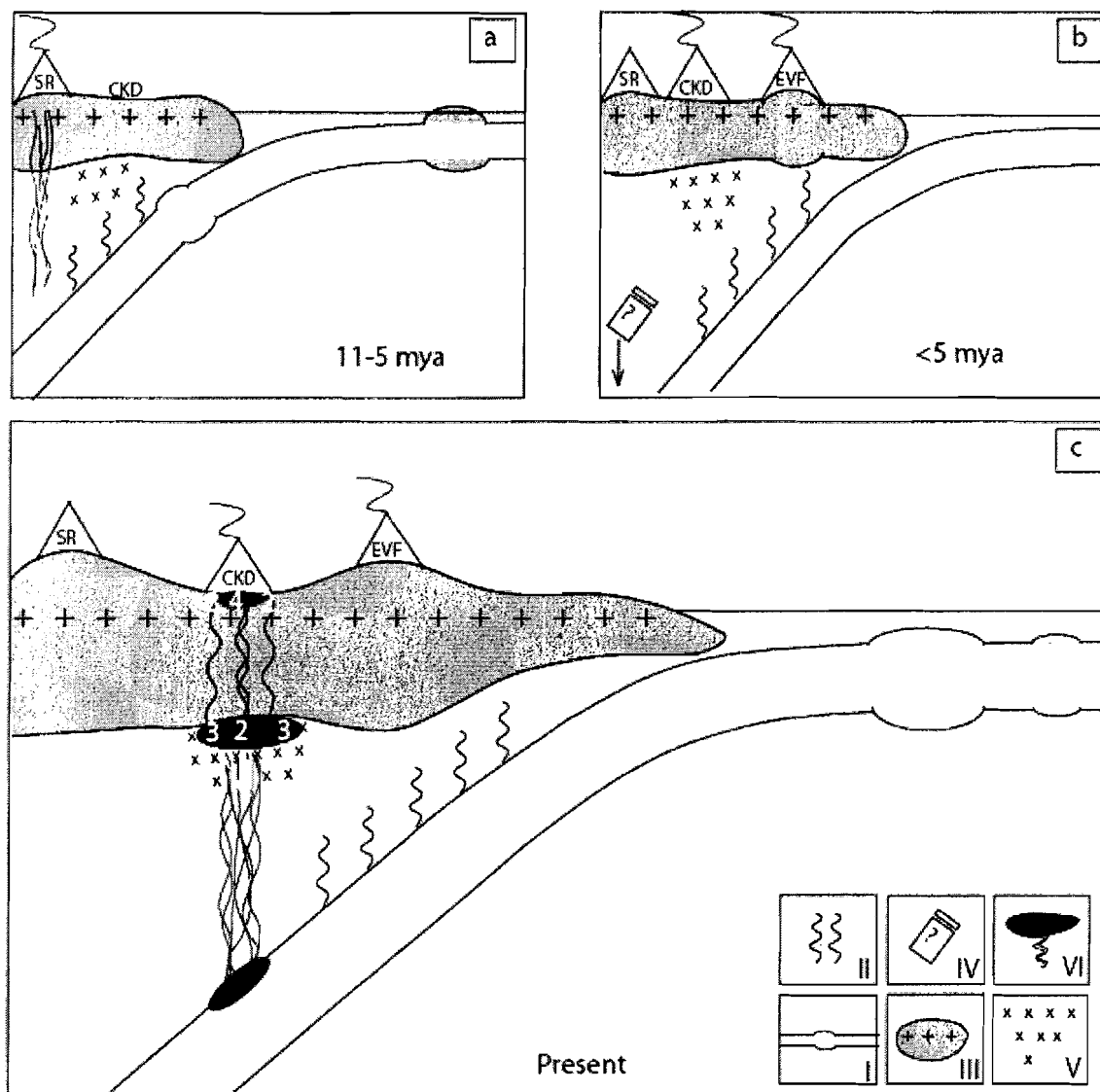


Figure 25. Schematic diagram of the evolution of Kamchatka and the corresponding processes involved from active volcanism at the Srdinny Ridge (SR) to the formation of Central Kamchatka Depression (CKD) volcanoes and the Eastern Volcanic Front (EVF) from (a) 11-5 ma, (b) <5ma, (c) present. In these diagrams: I-Hawaii-Emperor Seamounts, II-fluid, III-continental crust, IV-separated piece of subducted slab, V-melt, VI-serpentinized peridotite. In figure (c) four types of melt are present: 1-primary mantle melt source with 1a-normal mantle peridotite melt and 1b-high- $\delta^{18}\text{O}$ de-serpentinized mantle peridotite melt; 2-moderately high- $\delta^{18}\text{O}$, high-Mg basalt evolved primarily from 1a; 3-upper mantle high-Al, high- $\delta^{18}\text{O}$, high $^{87}\text{Sr}/^{86}\text{Sr}$ basalt evolved primarily from 1b; and 4-mixing of High-Mg and High-Al cumulates with basalt 2 and 3 upon rise.

subduction, and thus low temperature hydrothermal alteration of a larger fraction of the crust. This crust, on subduction, would therefore release a larger amount of high- $\delta^{18}\text{O}$ fluids, and thus possibly account for the high- $\delta^{18}\text{O}$ signature evidenced at Mt. Shasta (Martin et al. in prep). Therefore, for both cases we suggest that petrogenetic processes involve hydrous flux melting and larger than normal amounts of H_2O derived from subducted crust.

CHAPTER V

CONCLUSIONS

The results of this study have served to explain Klyuchevskoy's 1) voluminous, high-rate volcanism, 2) the unusual high- $\delta^{18}\text{O}$ signature of Klyuchevskoy and other CKD rocks and 3) the H_2O -rich nature of the high-Al high- $\delta^{18}\text{O}$ component. The processes involved in magma generation below Klyuchevskoy volcano are more complicated than previously interpreted. Major element data show the presence of both a high-Al and a high-Mg end member as well as intermediate products at Klyuchevskoy. These products are also enriched in $\delta^{18}\text{O}$, particularly the high-Al basalt. Olivine-hosted melt inclusions in high-Al samples are H_2O -rich, and contain up to 7.1 wt% water. Many samples have groundmass glass that is isotopically and chemically out of equilibrium with their olivines, indicating that olivine recycling is a likely process at Klyuchevskoy.

We have shown that subduction of the Hawaii-Emperor Seamount Chain, while a possibility for some $\delta^{18}\text{O}$ enrichment in the Klyuchevskoy Group area, cannot account for elevated $\delta^{18}\text{O}$ values found throughout the backarc. Simple fractionation of a primitive high-Mg, normal- $\delta^{18}\text{O}$ basalt will only increase the $\delta^{18}\text{O}$ of high-Al basalt on the order of 0.1-0.3‰, and cannot account for the several permil enrichment evident at Klyuchevskoy. Involvement of a pyroxenite mantle source was ruled out because of Mg/Fe, Ni, and Mn values which indicated a

peridotite source. Amphibolite assimilation models likewise could not provide a consistent model to account for observed Klyuchevskoy $\delta^{18}\text{O}$ - SiO_2 - H_2O values. Extensive examination of published values for ^{10}Be and $^{207}\text{Pb}/^{204}\text{Pb}$ $^{208}\text{Pb}/^{204}\text{Pb}$ ratios pertaining to sediment subduction shows no evidence of a significant contribution. Finally, fluid fluxing models require extremely high- $\delta^{18}\text{O}$ values for single-stage flux-melting and multi-stage flux melting, and would result in extremely high fluid mobile/immobile element signatures, which is not seen at Klyuchevskoy. Therefore, we present a hypothesis in which fluid flux melting of the mantle wedge creates primitive basaltic melts that rise and chemically interact with high- $\delta^{18}\text{O}$ peridotite in the uppermost mantle that was once hydrated and enriched as part of the forearc mantle prior to trench migration at ~ 5 m.y.a.

The formation of the high $\delta^{18}\text{O}$, high-Al and moderately high $\delta^{18}\text{O}$, high-Mg end members likely occur from the combination of varying degrees of two processes: (1) the release of fluid/melt (probably with moderately high $\delta^{18}\text{O}$) from the subducting slab resulting in flux melting of the mantle wedge (Portnyagin et al. 2007b) and (2) assimilation of an upper mantle $\delta^{18}\text{O}$ de-serpentinized mantle peridotite source, resulting in a high $\delta^{18}\text{O}$, high-Al melt. The high-Al magma may reflect a mixing of a substantial degree of high- $\delta^{18}\text{O}$ shallow mantle de-serpentinized peridotitic source, while the high-Mg source likely results primarily from the fluxing of water from the subducting slab material through the mantle peridotite, providing melt that is Mg-rich, more normal in $\delta^{18}\text{O}$, but still hydrous with H_2O concentrations up to 3.5 wt%. We consider that a subduction

rollback process is important in explaining the high- $\delta^{18}\text{O}$ hydrous basaltic magmas present in the CKD and worldwide.

APPENDIX A

MAJOR AND TRACE ELEMENT XRF ANALYSIS OF TEPHRA FROM

KLYUCHEVSKOY VOLCANO

Sample	KLV 4	KLV 5/1	KLV 5/3	KLV 5/4	KLV 5/5
Section	Cone D	KLV 05-05	KLV 05-05	KLV 05-05	KLV 05-05
Latitude	N56 08.527	N56 08.527	N56 08.527	N56 08.527	N56 08.527
Longitude	E160 48.054	E160 48.054	E160 48.054	E160 48.054	E160 48.054
Oxide, wt%	Un-normalized Major Elements (Weight %):				
SiO ₂	53.27	52.36	52.83	53.46	53.00
TiO ₂	0.91	0.98	1.04	1.03	1.03
Al ₂ O ₃	16.95	17.56	18.10	18.08	17.15
FeO*	8.00	7.93	7.92	8.03	8.40
MnO	0.16	0.16	0.16	0.16	0.16
MgO	6.88	5.02	4.83	5.16	6.35
CaO	9.22	8.04	8.11	8.31	8.74
Na ₂ O	3.27	3.52	3.76	3.74	3.32
K ₂ O	0.76	0.93	0.77	0.85	0.71
P ₂ O ₅	0.17	0.19	0.20	0.22	0.19
Sum	99.57	96.69	97.72	99.02	99.06
element, ppm	Un-normalized Trace Elements (ppm)				
Ni	65.3	35.5	25.5	27.3	51.2
Cr	197.1	52.5	37.5	38.4	119.8
Sc	30.6	24.3	26.6	26.1	29
V	242.8	235.9	257.1	251.7	245
Ba	264	380.2	274.2	297.3	240.7
Rb	12.2	14.9	10.4	12.5	10.7
Sr	328	338.2	319.9	359	318.9
Zr	78.9	88.6	91.7	92.9	92
Y	18.2	20.1	21.8	20.2	20.6
Nb	1.4	1.7	1.4	0.8	1.7
Ga	19.6	18.8	19.2	19.5	17.5
Cu	84.7	69.5	94.7	81.4	86.4
Zn	78.5	83	80.1	79.6	79.7
Pb	2.9	4	3.1	3.5	3
La	5.3	5.1	5	6.9	5.6
Ce	17.5	17.8	15.7	22.3	15.2
Th	2.4	3.4	3.1	3	1.8
Nd	12.8	11.7	11	14.4	11.6
K	0.632	0.773	0.638	0.702	0.593

Sample	KLV 5/6	KLV 5/8	KLV 5/10	KLV 5/12	KLV 5/13
Section	KLV 05-05	KLV 05-05	KLV 05-05	KLV 05-05	KLV 05-05
Latitude	N56 08.527	N56 08.527	N56 08.527	N56 08.527	N56 08.527
Longitude	E160 48.054	E160 48.054	E160 48.054	E160 48.054	E160 48.054
Oxide, wt%					
SiO ₂	52.76	51.48	52.73	52.71	54.88
TiO ₂	0.88	0.81	0.91	1.02	0.97
Al ₂ O ₃	16.55	13.87	16.86	17.34	18.12
FeO*	8.20	8.55	8.39	8.91	7.72
MnO	0.16	0.17	0.16	0.17	0.15
MgO	7.67	11.30	6.70	5.83	4.92
CaO	9.30	9.78	9.13	8.80	8.13
Na ₂ O	3.04	2.36	2.87	2.94	3.47
K ₂ O	0.68	0.56	0.70	0.77	1.00
P ₂ O ₅	0.16	0.14	0.15	0.17	0.18
Sum	99.40	99.01	98.62	98.66	99.55
element, ppm					
Ni	78.2	180.7	54.7	26.5	25.2
Cr	242.4	807.2	185.3	77.7	37.1
Sc	31.6	37.4	34.2	33.3	27.6
V	238.4	242.5	250.6	271.2	241.3
Ba	239.5	219.1	284.8	310.1	419.3
Rb	10.3	8.5	11.6	12	16.6
Sr	315.6	244.1	333.4	327.8	374.5
Zr	73.7	63.4	74.4	80.7	86.1
Y	18.1	16.7	17.1	22.2	20.1
Nb	1.6	1	1.8	1.3	2
Ga	16.4	15.3	18.7	17.4	18.9
Cu	75.2	76.9	68.2	41.4	39.2
Zn	75.1	73.1	78.2	83.6	81.2
Pb	3.3	2.4	3.6	2.8	4.3
La	2.6	3.8	5	5.3	5.3
Ce	13.5	14.6	14.9	10.6	18.3
Th	3.1	1.8	1.6	2.1	4.3
Nd	9.9	10.1	10.5	10.7	9.7
K	0.567	0.464	0.583	0.637	0.834

Sample	KLV 5/15	KLV 5/18a	KLV 5/19	KLV 5/20	KLV 5/22
Section	KLV 05-05	KLV 05-05	KLV 05-05	KLV 05-05	KLV 05-05
Latitude	N56 08.527	N56 08.527	N56 08.527	N56 08.527	N56 08.527
Longitude	E160 48.054	E160 48.054	E160 48.054	E160 48.054	E160 48.054
Oxide, wt%					
SiO ₂	51.23	53.44	54.50	53.78	54.34
TiO ₂	0.99	0.87	0.84	0.98	0.86
Al ₂ O ₃	16.94	14.85	16.79	17.34	15.99
FeO*	9.12	8.34	7.91	8.31	8.12
MnO	0.18	0.16	0.16	0.16	0.16
MgO	6.36	9.60	7.06	6.24	6.80
CaO	9.03	8.84	8.55	8.86	8.85
Na ₂ O	2.68	2.62	2.95	2.89	2.89
K ₂ O	0.63	0.77	0.85	0.80	0.85
P ₂ O ₅	0.16	0.17	0.18	0.15	0.18
Sum	97.30	99.67	99.79	99.51	99.05
element, ppm					
Ni	38.3	125.3	67.2	17.4	44.3
Cr	99.9	587.3	311.9	77.5	204.6
Sc	36.9	32.8	28	32.2	31.1
V	275.2	236	210	248	232.3
Ba	250.2	308.1	361.9	335.9	329.2
Rb	9.4	11.2	13.5	12.2	13
Sr	311.9	308.9	341.6	307.2	364.8
Zr	71.9	75	82.1	78.1	80.9
Y	20.1	19.3	20	20.2	17.8
Nb	2.2	1.4	1.3	1.1	1.3
Ga	18.6	16.3	18	17.8	18
Cu	87.7	30.7	26.9	20	57.9
Zn	80.3	79	91.7	84.2	78
Pb	2.7	3.5	3.3	3.5	3.1
La	4.3	3.3	5.8	5.5	4.5
Ce	16.1	13.2	17.7	10.3	16.8
Th	1.8	2.2	3	3.7	2.2
Nd	11.8	8.3	12.3	8.2	12.6
K	0.520	0.642	0.708	0.662	0.702

Sample	KLV 5/24	KLV 8	KLV 9	KLV 11/1	KLV 11/3
Section	KLV 05-05	Lepyoshka	nd	KLV 05-11	KLV 05-11
Latitude	N56 08.527	N56 08.992	N56 09.167	N56 09.167	N56 09.167
Longitude	E160 48.054	E160 47.710	E160 47.621	E160 47.621	E160 47.621
Oxide, wt%					
SiO ₂	57.01	52.67	52.77	52.14	53.48
TiO ₂	1.31	1.00	1.03	1.00	1.03
Al ₂ O ₃	17.39	15.97	16.63	17.29	17.35
FeO*	7.27	8.78	8.86	8.74	8.90
MnO	0.13	0.17	0.17	0.17	0.17
MgO	2.64	7.28	6.86	6.62	5.90
CaO	6.35	9.52	9.29	9.30	9.00
Na ₂ O	3.61	2.76	2.83	3.03	3.05
K ₂ O	2.17	0.72	0.74	0.58	0.78
P ₂ O ₅	0.61	0.16	0.17	0.15	0.16
Sum	98.49	99.02	99.34	99.03	99.84
element, ppm					
Ni	16.8	43.1	37.4	47.4	25.5
Cr	15.6	199	145.6	142.7	66.6
Sc	21.5	37	35.1	33.8	33.9
V	222.9	272.1	271.7	270.6	277.6
Ba	725.9	292.1	313.4	219.6	306.2
Rb	62.2	10.3	11.1	7.7	12.3
Sr	320.7	302.9	316.1	320.6	333.6
Zr	298.2	76.4	78.8	74	78.9
Y	42.5	21.9	21.4	20.3	21
Nb	6	1.8	1.6	1.5	1.4
Ga	20.8	16	19	17.4	19.2
Cu	203.2	42.8	40.1	73.8	42.4
Zn	88.4	81.8	83.6	80.4	84.3
Pb	9.5	3.6	2.8	1.2	3.4
La	22.8	7	6.7	1.7	5.7
Ce	62.3	17.2	13.1	12.2	19.1
Th	8.2	3.4	2.4	1.8	3.4
Nd	39.3	11.5	9.3	9.7	11.1
K	1.805	0.595	0.611	0.484	0.650

Sample	KLV 11/5	300-48	840-93/5-18	840-93/1-5	300-5/63
Section	KLV 05-11	300-75	840-93	840-93	300-75
Latitude	N56 09.167	nd	nd	nd	nd
Longitude	E160 47.621	nd	nd	nd	nd
Oxide, wt%					
SiO ₂	54.56	52.98	53.92	53.66	53.10
TiO ₂	0.97	1.03	1.06	0.91	1.03
Al ₂ O ₃	17.90	17.04	18.17	16.97	17.23
FeO*	7.67	8.85	8.25	8.34	8.35
MnO	0.15	0.17	0.16	0.16	0.16
MgO	4.98	5.96	5.09	6.77	6.28
CaO	8.12	8.89	8.30	8.68	8.80
Na ₂ O	3.42	2.94	3.78	3.24	3.32
K ₂ O	1.00	0.77	0.77	0.81	0.71
P ₂ O ₅	0.18	0.17	0.20	0.17	0.19
Sum	98.94	98.79	99.69	99.71	99.17
element, ppm					
Ni	25.1	27.6	28.5	55.7	49.3
Cr	40.9	73.3	34.1	133.7	128.3
Sc	27.3	32.9	27.3	28.9	29.5
V	238.3	275.4	263.3	237.7	250.6
Ba	415.3	306.2	272.5	334.4	241
Rb	16.3	12.1	12.6	12.8	10.2
Sr	369.7	326.1	320	317.5	319.5
Zr	85.5	79.2	92.4	79.4	92.5
Y	19.8	20.8	21.7	19.4	21
Nb	1.4	1.2	1.8	0.6	1.3
Ga	18.7	17.9	20.5	16.4	19.3
Cu	35.9	39.6	84.8	58.3	84.4
Zn	81.7	83.9	79.8	80.7	80
Pb	3.7	3.2	3.5	2.9	3.8
La	6.3	6.7	5.8	3.6	4.1
Ce	16.9	15.1	17.4	14.9	14.7
Th	2.8	3	2.5	3.1	1.5
Nd	12.9	10.2	14	8.8	12
K	0.833	0.640	0.635	0.674	0.592

APPENDIX B
FIELD NOTES FROM SAMPLE COLLECTING AROUND KLYUCHEVSKOY
VOLCANO JULY/AUGUST 2005

KLV	Sample of	Location	Latitude	Longitude	Type	Ave grain size	Unit thickness	Visible Phases or lithics	~Age Yrs BP
1		Near shack	N56 08.750	E160 47.945	lava	nr	nr	ol	200
2		Near shack	N56 08.726	E160 48.087	lava	nr	nr	pl	1500
3	Cone D?	River D Sect. 1	N56 08.562	E160 48.228	lava	nr	nr	ol; px	2450
4	Cone D	River D Sect. 1	N56 08.527	E160 48.054	tephra	nr	~6m	ol; px	2300
5	1	River D Sect. 1	N56 08.527	E160 48.054	scoria	0.4cm	2-3cm		50
	2	River D Sect. 1	N56 08.527	E160 48.054	scoria	nr	1cm	pl	350
	3	River D Sect. 1	N56 08.527	E160 48.054	scoria	0.4cm	2cm		1100
	4	River D Sect. 1	N56 08.527	E160 48.054	scoria	0.4cm	3cm		1200
	5	River D Sect. 1	N56 08.527	E160 48.054	scoria	1cm	nr		1600
	6	Cone D?	River D Sect. 1	E160 48.054	scoria	0.2cm	13cm	ol	2500
	7	River D Sect. 1	N56 08.527	E160 48.054	ash	0.1-0.2cm	nr		2600
	8	River D Sect. 1	N56 08.527	E160 48.054	scoria	0.2cm	5cm	ol	2650
	9	River D Sect. 1	N56 08.527	E160 48.054	scoria	0.1cm	4cm		2700
	10	River D Sect. 1	N56 08.527	E160 48.054	scoria	0.8cm	4cm		3000
	11	River D Sect. 1	N56 08.527	E160 48.054	scoria	nr	13cm	ol	3100
	12	River D Sect. 1	N56 08.527	E160 48.054	scoria	0.5cm	18cm	li	3400
	13	River D Sect. 1	N56 08.527	E160 48.054	scoria	0.8cm	4cm	li	3600
	14	River D Sect. 1	N56 08.527	E160 48.054	scoria	nr	nr		4300
	15	River D Sect. 1	N56 08.527	E160 48.054	scoria	0.4-0.5cm	1.5cm		4750
	16	River D Sect. 1	N56 08.527	E160 48.054	scoria	0.1-0.2cm	4cm		5100
	17	River D Sect. 1	N56 08.527	E160 48.054	ash	0.3cm	3-5cm		5550
	18a	River D Sect. 1	N56 08.527	E160 48.054	scoria	0.3cm	25cm		5800
	18b	River D Sect. 1	N56 08.527	E160 48.054	lithics	nr	25cm		5800
	19	River D Sect. 1	N56 08.527	E160 48.054	scoria	0.1-0.3cm	6cm		5900
	20	River D Sect. 1	N56 08.527	E160 48.054	scoria	0.5cm	2cm		6400
	21	River D Sect. 1	N56 08.527	E160 48.054	scoria	0.1-0.3cm	1cm	pl	7100
	22	River D Sect. 1	N56 08.527	E160 48.054	scoria	nr	2-3cm		7250

KLV	Sample of	Location	Latitude	Longitude	Type	Average grain size	Unit thickness	Visible Phases	~Age Yrs BP
5	23	River D Sect. 1	N56 08.527	E160 48.054	sand	nr	1cm	mm	7700
	24	River D Sect. 1	N56 08.527	E160 48.054	scoria	2cm	55cm	li	8550
	24b	River D Sect. 1	N56 08.527	E160 48.054	lithics	nr	55cm	li	8550
	25a	River D Sect. 1	N56 08.527	E160 48.054	scoria	nr	1-2cm	pl	8650
	25b	River D Sect. 1	N56 08.527	E160 48.054	pl	nr	1-2cm		8650
6	PIIP	PIIP Lava Flow	N56 09.113	E160 47.746	nr	nr	nr	ol	41
7		nd	N56 08.992	E160 47.710	lava	nr	nr	ol; px; pl	41-200
8		nd	N56 08.992	E160 47.710	scoria	nr	~6m		3400
9		Mud waterfall	N56 09.167	E160 47.621	scoria	1cm	~0.5m		3250
10	Bulochka	Mud waterfall	N56 09.167	E160 47.621	lava	nr	nr		3200
11	1	Riverbank #2	N56 09.167	E160 47.621	scoria	0.4cm	2cm		1600
	2	Riverbank #2	N56 09.167	E160 47.621	scoria	nr	2cm		2700
	3	Riverbank #2	N56 09.167	E160 47.621	scoria	nr	nr		3250
	4	Riverbank #2	N56 09.167	E160 47.621	scoria	0.1cm	4cm		3400
	5	Riverbank #2	N56 09.167	E160 47.621	scoria	nr	3cm	li	3600
12		Ravine #1	N56 09.064	E160 46.903	lava	nr	nr		nd
13		Ravine #1	N56 09.064	E160 46.903	scoria	nr	nr		8550
14		Ravine #1	N56 09.167	E160 47.621	lava	nr	nr	pl	nd
15	1	Riverbank #3	N56 09.201	E160 48.009	sand	0.2cm	7cm	pl	400
	2	Riverbank #3	N56 09.201	E160 48.009	scoria	0.8cm	3-6cm		750
16	Bezymianny	nd	N56 08.819	E160 48.102	ash	nr	nr		51
17	Klyuchevskoy	nd	N56 08.819	E160 48.102	ash	nr	nr		13
18	SH2	Riverbank #1	N56 08.527	E160 48.054	ash	nr	nr		9950
19	SH3	Riverbank #1	N56 08.527	E160 48.054	ash	nr	nr		1450
20	Cone E/I	Cone E/I	N56 07.104	E160 45.040	scoria	nr	nr	ol	1950
21	Cone O	Cone O	N56 07.221	E160 45.268	lava	nr	nr	ol	150
22	Belyanankin	nd	N56 07.853	E160 45.405	lava	nr	nr		100
23	Levashov	Cone Levashov	N56 07.747	E160 46.114	scoria	nr	nr	ol	2300

KLV	Sample of	Location	Latitude	Longitude	Type	Average grain size	Unit thickness	Visible Phases	~Age Yrs BP
23b	Levashov	Cone Levashov	N56 07.747	E160 46.114	ol	nr	nr	ol	2300
24	Cone J [I]	Cone J [I]	N56 06.974	E160 48.397	scoria	0.2cm	nr	ol	2650
25	Bylinkina	Cone Bylinkina	N56 06.618	E160 49.357	bomb?	nr	nr		54
26	Shmalev	Cone Shmalev	N56 06.737	E160 49.942	scoria	nr	nr		1700
27	Bering Cone	Bering Cone	N56 06.911	E160 50.127	scoria	nr	nr		3400
28	Cone M?	Waterfall	N56 07.158	E160 49.629	lava	nr	nr	ol	2700
29	Cone I/E?	Riverbank #4	N56 07.180	E160 49.598	scoria	nr	1.66m		2475
30	Ploski	Riverbank #4	N56 11.258	E160 52.257	lava	nr	nr	pl	>8600
31	Klyuchevskoy	Riverbank #4	N56 11.531	E160 52.970	lava	nr	nr	ol	>8600
32		Riverbank #4	N56 11.522	E160 53.102	lava	nr	nr	pl	8450
33		Riverbank #4	N56 11.258	E160 52.257	lava	nr	nr		>8600
34	SH3	Kliuchi	N56 18.634	E160 53.459	scoria	nr	nr		1450
35		Kliuchi	N56 19.622	E160 50.529	lava	nr	nr	pl	nd
36		Kozyrevsk	N56 02.776	E159 51.148	lava	nr	nr		nd

BIBLIOGRAPHY

Almeev RR, Geokhimiya magmatizma vulkana Bezymianny: Priznaki mantiinogo istochnika i uslovia fraktsionirovaniya iskhodnoi magmi [Geochemistry of magmatism of Bezymianny volcano: mantle source and conditions of fractionation of the primary magma] in Russian. Dissertation defended at Vernadsky Institute of Geochemistry

Anderson, AT (1973) The before-eruption water content of some high-alumina magmas. *Bulletin of Volcanology* 37:530-552

Ariskin AA, Barmina GS, Ozerov AY, Nielsen RL (1995) Genesis of High-Alumina Basalts of Klyuchevskoy Volcano. *Petrology* 3/5:496-521

Bailey JC, (1996) Role of subducted sediments in the genesis of Kurile–Kamchatka island arc basalts: Sr isotopic and elemental evidence, *Geochimica Cosmochimica Acta* 30:289-321

Bindeman IN, Vinogradov VI, Valley JW, Wooden JL, Natal'in BA, (2002) Archean Protolith and Accretion of Crust in Kamchatka: SHRIMP Dating of Zircons from Sredinny and Ganal Massifs. *The Journal of Geology* 110:271–289

Bindeman IN, Ponomareva VV, Bailey JC, Valley JW, (2004) Volcanic arc of Kamchatka: a province with high-delta O-18 magma sources and large-scale O-18/O-16 depletion of the upper crust. *Geochimica Cosmochimica Acta* 68/4:841-865

Bindeman IN, Eiler JM, Yogodzinski G, Tatsumi Y, Stern C, Grove T, Portnyagin M, Hoernle K, Danyushevsky L (2005) Oxygen isotope evidence for slab melting in modern and ancient subduction zones. *Earth and Planetary Science Letters* 235:480-496

Bindeman IN, Sigmarsson O, Eiler JM (2006) Time constraints on the origin of large volume basalts derived from O-isotope and trace element mineral zoning and U-series disequilibria in the Laki and Grímsvötn volcanic system. *Earth and Planetary Science Letters* 245:245-259

Braitseva OA, Ponomareva VV, Sulerzhitsky LD, Melekestsev IV, Bailey JC (1997) Holocene key-marker tephra layers in Kamchatka, Russia. *Quaternary Research* 47: 125-139

Chiba H, Chacko T, Clayton RN, Goldsmith JR (1989) Oxygen isotope fractionations involving diopside, forsterite, magnetite, and calcite: Application to geothermometry. *Geochimica Cosmochimica Acta* 53:2985-2995

Churikova T, Dorendorf F, Worner G (2001) Sources and fluids in the mantle wedge below Kamchatka, evidence for across-arc geochemical variation. *Journal of Petrology* 42: 1567-1593

Danyushevsky LV, McNeill AW, Sobolev AV (2002) Experimental and petrological studies of melt inclusions in phenocrysts from mantle-derived magmas: and overview of techniques, advantages and complications. *Chemical Geology* 183:5-24

DePaulo DJ, (1981) Trace element and isotopic effects of combined wall rock assimilation and fractional crystallization. *Earth and Planetary Science Letters* 53:189–202

Dixon JE, Pan V (1995) Determination of the molar absorptivity of dissolved carbonate in basanitic glass. *American Mineralogist* 80:1339-1342

Dixon JE, Stolper EM, Holloway JR (1995) An experimental study of water and carbon dioxide solubilities in mid-ocean ridge basaltic liquids. Part I: calibration and solubility models. *Journal of Petrology* 36/6:1607-1631

Dorendorf F, Wiechert U, Worner G (2000) Hydrated sub-arc mantle: A source for the Klyuchevskoy volcano, Kamchatka/Russia. *Earth and Planetary Science Letters* 175: 69-86

Duggen S, Portnyagin M, Baker J, Ulfbeck D, Hoernle K, Garbe-Schonberg D, Grassineau N (2007) Drastic shift in lava geochemistry in the volcanic-front to rear-arc region of the Southern Kamchatkan subduction zone: Evidence for the transition from slab surface dehydration to sediment melting. *Geochimica Cosmochimica Acta* 71:452-480

Ducea MN, Barton MD (2007) Igniting flare-up events in Cordillieran arcs. *Geology* 35: 1047-1050

Ghiorso MS, Sack Ro (1995) Chemical mass transfer in magmatic processes. 4. A revised and internally consistent thermodynamic model for the interpolation and extrapolation of liquid-solid equilibria in magmatic systems at elevated temperatures and pressures. *Contributions to Mineralogy and Petrology* 119(2-3):197-212.

Gill JB (1981) *Orogenic Andesites and Plate Tectonics*. Springer-Verlag.

- Gorbatov A, Kostoglodov V, Suarez G, Gordeev E (1997) Seismicity and structure of the Kamchatka subduction zone. *Journal of Geophysical Research* 102:17833-17898
- Gorbatov A, Domínguez J, Suárez G, Kostoglodov V, Zhao D, Gordeev E (1999) Tomographic imaging of the *P*-wave velocity structure beneath the Kamchatka peninsula. *Geophysical Journal International* 137(2):269-279
- Gorbatov A, Fukao Y, Widiyantoro S, Gordeev E (2001) Seismic evidence for a mantle plume oceanward of the Kamchatka-Aleutian trench junction. *Geophysics Journal International* 146:282-288
- Grove TL, Parman SW, Bowring SA, Price RC, Baker MB (2002) The role of an H₂O-rich fluid component in the generation of primitive basaltic andesites and andesites from the Mt. Shasta region, N. California. *Contributions to Mineralogy and Petrology* 142:375-396
- Grove TL, Chatterjee N, Parman SW, Medard E (2006) The influence of H₂O on mantle wedge melting. *Earth and Planetary Science Letters* 249(1-2):74-89
- Hildreth W, Moorbath S (1988) Crustal contributions to arc magmatism in the Andes of Central Chile. *Contributions to Mineralogy and Petrology* 98:455- 489
- Kelsey (1965) Calculation of the C.I.P.W. norm. *Mineralogical magazine* 34:276-282
- Kersting AB, Arculus RJ, (1994) Klyuchevskoy Volcano, Kamchatka Russia- The role of High-flux recharged, tapped, and fractionated magma chamber(s) in the genesis of high-Al₂O₃ from high MgO basalt. *Journal of Petrology* 35/1:1-41
- Kersting AB, Arculus RJ (1995) Pb isotope composition of Klyuchevskoy volcano, Kamchatka and North Pacific sediments: Implications for magma genesis and crustal recycling in the Kamchatkan arc. *Earth and Planetary Science Letters* 136/3-4:133-148
- Khrenov AP, Dvigalo VN, Kirsanov IT, Fedotov SA, Gorel'chik VI, Zharinov, NA (1991) Klyuchevskoy volcano In: Fedotov SA, Masurenkov, YP (eds) *Active volcanoes of Kamchatka*, vol 1. Moscow, Nauka Publishers, 104-153
- Khubunaya SA, Gontovaya LI, Sobolev AV, Niskous I (2007) Magma chambers beneath Klyuchevskoy group volcanoes. *Volcanology and Seismology* 2:32-54
- Konstantinovskaia EA (2001) Geodynamics of an Early Eocene arc-continent collision reconstructed from the Kamchatka Orogenic Belt, NE Russia. *Tectonophysics* 325: 87-105

Lees JM, Symons N, Chubarova O, Gorelchik V, Ozerov A (2007) Tomographic Images of Klyuchevskoy Volcano P-wave Velocity In: Eichelberger J, Izbekov P, Kasahara M, Lees J, Gordeev E (eds) *Volcanism and tectonics of the Kamchatka Peninsula and adjacent arcs*, American Geophysical Union Monograph Series, in press

Levin V, Shapiro N, Park J, Ritzwoller M, (2002) Seismic evidence for catastrophic slab loss beneath Kamchatka. *Nature* 418:763-767

Manea VC, Manea M, Clark S (2007) Thermal models beneath Kamchaka and the Pacific plate rejuvenation from a mantle plume impact. In: Eichelberger J, Izbekov P, Kasahara M, Lees J, Gordeev E (eds) *Volcanism and tectonics of the Kamchatka Peninsula and adjacent arcs*, American Geophysical Union Monograph Series, in press

Melekestsev IV (1980) *Volcanism and Relief Formation*. Nauka, Moscow (in Russian).

Mironov NL, Portnyagin MV, Pletchov PY, Khubunaya SA (2001) Final Stages of Mama Evolution in Klyuchevskoy Volcano, Kamchatka: Evidence from Melt Inclusions in Minerals of High-Alumina Basalts. *Petrology* (9/1):51-69.

Muehlenbachs K (1986) Alteration of the oceanic crust and the ^{18}O history of seawater, In: JW Valley, HP Taylor, JR O'Neil Jr (eds), *Stable Isotopes in High Temperature Geological Processes*. *Reviews in Mineralogy*, 16:425-444

Newman S, Lowenstern JB (2002) VolatileCalc: a silicate melt-H₂O-CO₂ solution model written in Visual Basic for excel. *Computers & Geosciences* 28:597-604

Nichols ARL, Wysoczanski RJ (2007) Using micro-FTIR spectroscopy to measure volatile contents in small and unexposed inclusions hosted in olivine crystals. *Chemical Geology* 242(3-4):371-384

Ochs FA, Lange RA (1999) The density of hydrous magmatic liquids. *Science* 283:13414-1317

Osipenko AB, Sidorov EG, Shevchenko SS, Konilov AN, Rassulov VA, Rudashevskii NS (2007) Geochemistry and U-Pb Geochronology of Zircon in Garnet Amphibolites from Kamchatkskii Cape Peninsula, Eastern Kamchatka. *Geochemistry International* 45/3:226-234

Ozerov AY, Ariskin AA, Kyle P, Bogoyavlenskaya GE, Karpenko SF (1997) Petrological–Geochemical Model for Genetic Relationships between Basaltic and Andesitic Magmatism of Klyuchevskoi and Bezmyannyi Volcanoes, Kamchatka. *Petrology* (5/6):614-635

- Ozerov AY (2000) The evolution of high-alumina basalts of the Klyuchevskoy volcano, Kamchatka, Russia, based on microprobe analyses of mineral inclusions. *Journal of Volcanology and Geothermal Research* 95:65–79
- Pineau F, Semet MP, Grassineau N, Okrugin VM, Javoy M (1999) The genesis of the stable isotope (O,H) record in arc magmas: the Kamchatka's case. *Chemical Geology* 62: 157-176
- Piyp VB, Yefimova YA (1993) Seismic sections of the earth's crust under volcanoes of Kamchatka. *International Geology Review* 35:170-177
- Pokrovsky BG, Volynets ON (1999) Oxygen-isotope geochemistry in volcanic rocks of the Kurile-Kamchatka arc. *Petrology* 7:227-251
- Portnyagin M, Hoernle K, Avdeiko GP, Hauff F, Werner R, Bindeman IN, Uspensky VS, Garbe-Schönberg, CD (2005) Transition from arc to oceanic magmatism at the Kamchatka-Aleutian junction. *Geology* (33/1): 25-28
- Portnyagin M, Hoernle K, Plechov P, Mironov N, Khubunaya S (2007a) Constraints on mantle melting and composition and nature of slab components in volcanic arcs from volatiles (H₂O, S, Cl, F) and trace elements in melt inclusions from the Kamchatka Arc. *Earth and Planetary Science Letters* 255:53-69
- Portnyagin, M, Bindeman, IN, Hoernle K, Hauff F (2007b) Geochemistry of primitive lavas of the Central Kamchatka Depression: Magma Generation at the Edge of the Pacific Plate. In: Eichelberger J, Izbekov P, Kasahara M, Lees J, Gordeev E (eds) *Volcanism and tectonics of the Kamchatka Peninsula and adjacent arcs*, American Geophysical Union Monograph Series, in press
- Savin SM, Lee L (1988) Isotopic studies of hydrous phyllosilicates. In: Bailey SW (ed) *Hydrous Phyllosilicates (exclusive of micas)*. *Reviews in Mineralogy* 19:189-233
- Sisson TW, Bronto S (1998) Evidence for pressure-release melting beneath magmatic arcs from basalt at Galunggung, Indonesia. *Nature* 391:883-886
- Sobolev AV, Shimizu N (1993) Ultra-depleted primary melt included in an olivine from the Mid-Atlantic Ridge. *Nature* 363:151-154.
- Sobolev AV (2007) The amount of recycled crust in sources of mantle-derived melts. *Science* 316:412-417

- Spera FJ, Bohrson, WA (2002) Energy-Constrained Open-System Magmatic Processes III: Energy-Constrained Recharge, Assimilation and Fractional Crystallization (EC-RAFC). *Geochemistry, Geophysics, Geosystems* 3(12):8001, doi:10.1029/2002GC000315
- Staudigel H, Davies GR, Hart SR, Marchant KM, Smith BM (1995) Large-scale isotopic Sr, Nd and O isotopic anatomy of altered oceanic crust-DSP/ODP sites 417/418. *Earth and Planetary Science Letters* 130:169-185
- Sun SS, McDonough WF (1989) Chemical and isotopic systematics of oceanic basalts: Implications for the mantle composition and processes. In: *Magmatism in the Ocean Basin*, vol 42 *Geol Soc Sp Publi*, 313-345
- Tera F, Brown L, Morris J, Sacks IS, Klein J, Middletown R (1986) Sediment incorporation in island-arc magmas: Inferences from ^{10}Be . *Geochimica Cosmochimica Acta* 4:535-550
- Volynets ON (1994) Geochemical types, petrology and genesis of Late Cenozoic volcanic rocks from the Kurile-Kamchatka island-arc system. *International Geology Review* 36/4: 373-405
- Wallace PJ (2005) Volatiles in subduction zone magmas: concentrations and fluxes based on melt inclusion and volcanic gas data. *Journal of Volcanology and Geophysical Research* 140:217-240
- Wenner DB, Taylor HP Jr (1971) Temperatures of serpentinization of ultramafic rocks based on $^{18}\text{O}/^{16}\text{O}$ fractionation between coexisting serpentine and magnetite. *Contributions to Mineralogy and Petrology* 32:165-185
- Yogodzinski GM, Lees JM, Churikova TG, Dorendorf F, Woerner G, Volynets ON (2001) Geochemical evidence for the melting of subducting oceanic lithosphere at plate edges. *Nature* 404:500-50